Hydrodynamics of Meander Bends in Intertidal Mudflats: a Field Study From the Macrotidal Yangkou Coast, China

Chao Gao[1,2], A. Finotello[2,*], A. D'Alpaos[2], M. Ghinassi[2], L. Carniello[3], Yupeng Pan[1], Dezhi Chen[4], and Ya Ping Wang[1,5*]

[1]*Ministry of Education Key Laboratory for Coast and Island Development, School of Geographic and Oceanographic Sciences, Nanjing University, Nanjing, 210093, China*

[2]*Dept. of Geosciences, University of Padova, via Gradenigo 6, IT-35131, Padova (Italy)*

[3]*Dept. of Civil, Environmental, and Architectural Engineering, University of Padova, via Marzolo 9, IT-35131, Padova (Italy)*

[4]*Key Laboratory of Tropical Marine Ecosystem and Bioresource, Fourth Institute of Oceanography, Ministry of Natural Resources, Beihai, 53600, China*

[5]*State Key Laboratory of Estuarine and Coastal Research, School of Marine Sciences, East China Normal University, Shanghai, 200062, China*

*Corresponding authors:

Ya Ping Wang (ypwang@nju.edu.cn); Alvise Finotello (alvise.finotello@unipd.it)

Key Points

- Hydroacoustic measurements in a macrotidal-mudflat meandering channel show pronounced differences between above and below-bankfull stages
- Offset between streamwise and cross-stream velocity maxima limit advection of secondary flows and hinder curvature-induced helical flows
- High velocities and sustained seepage flows at late-ebb stages likely exert stronger controls than helical flows on meander morphodynamics

Keywords

Tidal Meanders; Mudflat; Hydroacoustic; Helical flow; Secondary circulations; Flow Separation

Abstract

Meandering channels are ubiquitous features in intertidal mudflats and play a key role in the eco-morphosedimentary evolution of such landscapes. However, the hydrodynamics and morphodynamic evolution of these channels are poorly known, and direct flow measurements are virtually nonexistent to date. Here, we present new hydroacoustic data collected synchronously at different sites along a mudflat meander located in the macrotidal Yangkou tidal flat (Jiangsu, China) over an 8-day period. The studied bend exhibits an overall dominance of flood flows, with velocity surges of about 0.8 m/s occurring immediately below the bankfull stage during both ebb and flood tides. Unlike salt-marsh channels, velocities attain nearly-constant, sustained values as long as tidal flows remain

confined within the channel, and reduce significantly during overbank stages. In contrast, curvature-induced cross-sectional flows are more pronounced during overbank stages. Thus, a phase lag exists between streamwise and cross-stream velocity maxima, which limits the transfer of secondary flows and likely hinders the formation of curvature-induced helical flows along the entire meander length. Our results support earlier suggestions that the morphodynamics of intertidal mudflat meanders does not strongly depend on curvature-induced helical flows, and is most likely driven by high velocities and sustains seepage flows at late-ebb stages, as well as by other non-tidal processes such as waves and intense rainfall events. By unraveling complex flow structures and intertwined morphodynamic processes, our results provide the first step toward a better understanding of intertidal mudflat meanders, with relevant implications for their planform characteristics and dynamic evolution.

1 Introduction

Tidal mudflats are among the most extensive coastal ecosystems worldwide (Murray et al., 2019; Murray et al., 2022). They are low-gradient intertidal landforms typically occurring in sediment-rich environments (Gao, 2019; Klein, 1985; Rogers & Woodroffe, 2015) characterized by large tidal oscillations relative to characteristic wind-wave heights (e.g., Friedrichs, 2011; Klein, 1985; Morales, 2022). Tidal mudflats are extremely important from both ecological and economic perspectives thanks to the broad range of ecosystem services they provide (Passarelli et al., 2018), including, nutrient cycling, carbon sequestration, water filtering, habitat provision for wildlife, food production, recreational activities, and cultural services (Choi, 2014; Friedrichs & Perry, 2001; Kim et al., 2000; Kirwan & Megonigal, 2013; Pilkey & Cooper, 2004; Shi et al., 2018; Temmerman et al., 2013; Vousdoukas et al., 2020).

The morphosedimentary evolution of tidal mudflats is intimately linked to the morphodynamics of the extensive networks of tidal channels that cut through them (Figure 1). These channels are typically meandering in planform to a greater or lesser degree (Choi, 2014; Friedrichs, 2011; Gao, 2019; Hughes, 2012), and play a primary role in regulating the exchanges of water, sediments, nutrients, and biota with the open sea (Coco et al., 2013; D'Alpaos et al., 2005), thus exerting a prominent control on the eco-geomorphology of the tidal-flat ecosystem as a whole (Choi, 2014; Hughes, 2012; Wells et al., 1990). Besides, lateral migration of meandering channels critically affects both the sedimentology and stratigraphy of tidal-flat systems, especially in terms of preservation potential (Choi, 2011; Choi et al., 2013; Ghinassi et al., 2019; Kleinhans et al., 2009). Indeed, mudflat tidal channels are typically preserved in the fossil record either as laterally-accreting, heterolithic point bars or through the infilling of abandoned channels generated either from meander cutoff or channel avulsion (Brivio et al., 2016; Choi, 2010; Cosma et al., 2020; Hughes, 2012; Sisulak & Dashtgard, 2012).

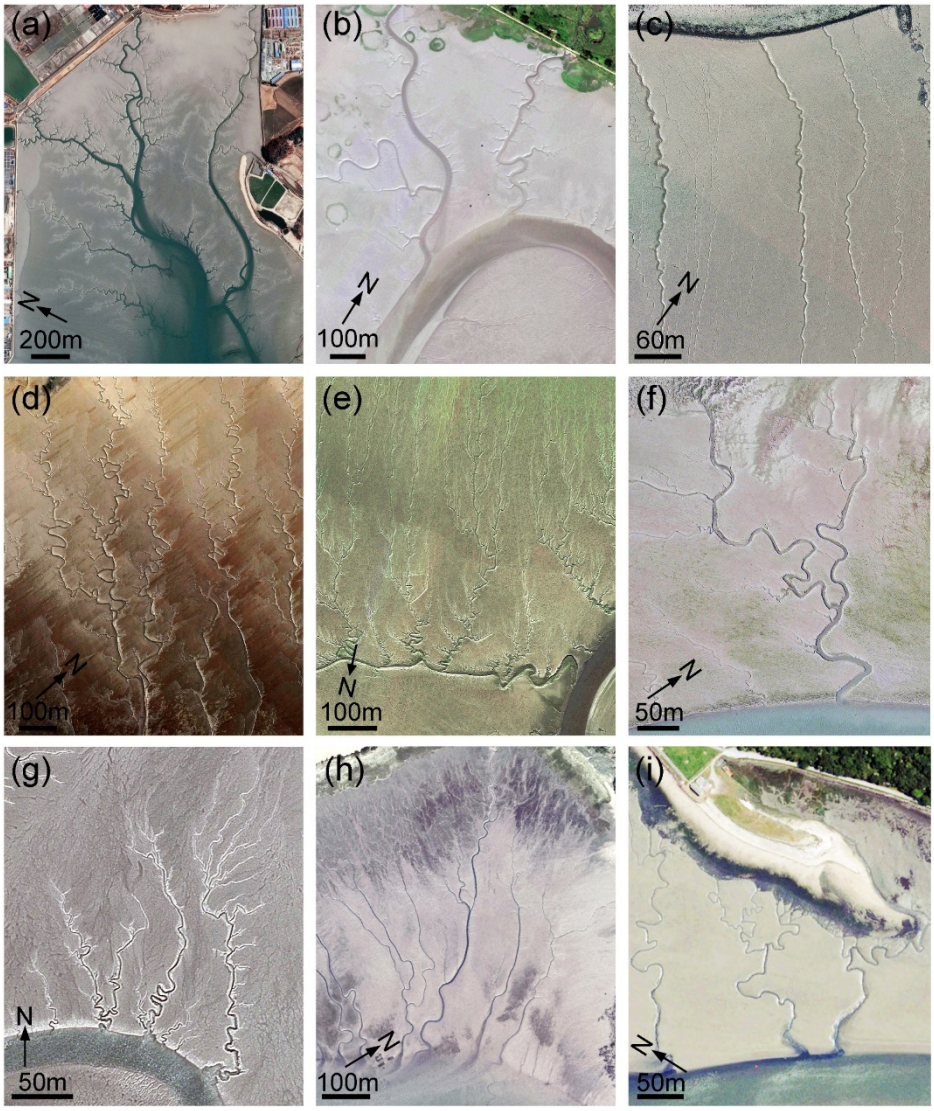

Figure1. Examples of meandering channels in tidal mudflats along the World's coast. (a) Baegmihang Port, South Korea (37°09 N, 126°40 E; ©Google, TerraMetrics; imagery date: March 14, 2019). (b) Boseong Bay, South Korea (34°52 N, 127°30 E; ©Google, Maxar Technologies; imagery date: August 30, 2020). (c) Cardiff Flats, England (51°28 N, 3°08 W; ©Google, Maxar Technologies; imagery date: July 11, 2013). (d) Fundy Bay, Canada (45°45 N, 64°38 E; ©Google, Maxar Technologies; imagery date: May 21, 2017). (e) Mühlenberger Loch, Germany (53°32 N, 9°48 E; ©Google, CNES/Airbus; imagery date: April 22, 2020). (f) The Wadden Sea, Germany (53°41 N, 8°02 E; ©Google, Maxar Technologies; imagery date: September 25, 2016). (g) I'Épinay Estuary, France

(47°31 N, 2°36 W; ©Google, Maxar Technologies; imagery date: March 19, 2011). (h) Lanveur Bay, France (48°21 N, 4°17 W; ©Google, Landsat/Copernicus; imagery date: January 01, 2005). (i) Morlaix Bay, France (48°38 N, 3°51'W; ©Google, TerraMetrics; imagery date: January 01, 2005).

In spite of their prominence and ubiquity, however, meandering channels in tidal mudflats are still poorly studied especially from a hydrodynamic standpoint. Previous field measurements of flow fields in tidal meanders focused primarily on either tidally-influenced fluvial reaches, where flow dynamics are largely influenced by river discharges and density-stratification effects (Chant, 2002; Keevil et al., 2015; Kranenburg et al., 2019; Somsook et al., 2020), or on intertidal channels dissecting vegetated salt marshes and mangrove swamps (Finotello, Ghinassi, et al., 2020; Horstman et al., 2021). In contrast, field studies on tidal meanders wandering through unvegetated intertidal mudflats are still scarce (Choi et al., 2013; Kleinhans et al., 2009), and flow velocity measurements are virtually nonexistent to date. This is a critical knowledge gap because significant differences might exist in terms of flow fields between tidal channels wandering through vegetated and unvegetated intertidal plains, especially concerning overbank stages (i.e., water levels that exceed the channel bankfull capacity). Magnitudes of overbank velocities in vegetated settings dominated by turbulence and friction are typically a magnitude lower than those observed on unvegetated mudflats (Bouma et al., 2005; Christiansen et al., 2000; D'Alpaos et al., 2021; Friedrichs, 2011; Hughes, 2012; Rinaldo et al., 1999a; Sullivan et al., 2015). Besides, overbank stages are more frequent in mudflats than in salt marshes, owing to the relatively lower position occupied by mudflat channel banks within the intertidal frame. As such, stage-velocity relations in mudflat tidal channels can differ greatly from those observed in vegetated marshes and mangrove forests, and overbank stages might have stronger control on tidal channel morphodynamics (D'Alpaos et al., 2021; Hughes, 2012; Kearney et al., 2017; McLachlan et al., 2020; Sgarabotto et al., 2021), potentially justifying the observed morphological differences of tidal channel networks in distinct vegetational settings (Geng et al., 2021; Kearney & Fagherazzi, 2016; Schwarz et al., 2022). These differences in landforming hydrodynamic processes are also likely to affect the development of curvature-induced helical flow that is typically related to the development and growth of meander bends in both rivers and salt-marsh tidal channels (Azpiroz-Zabala et al., 2017; Finotello, Ghinassi, et al., 2020; Keevil et al., 2015; Kranenburg et al., 2019; Nidzieko et al., 2009; Thorne et al., 1985). Such helical flow forms as a consequence of secondary (i.e., cross-sectional) circulations, oriented toward the inner and outer bank in the near-bed and near-surface zone, respectively, which result from the imbalance between the upward-increasing centrifugal forces and the lateral pressure gradients created by the curvature-induced superelevation of the water surface at the outer bank (Engelund, 1974; Prandtl, 1926; Rozovskiĭ, 1957; Solari et al., 2002). The downstream advection of secondary circulations operated by the main streamwise flow produces a helical flow, as extensively documented in a variety of field (Dietrich & Smith, 1983; Dinehart & Burau, 2005; Frothingham

& Rhoads, 2003), laboratory (Blanckaert, 2011; Liaghat et al., 2014), and numerical studies (Blanckaert & de Vriend, 2003; Bridge & Jarvis, 1982; Ferguson et al., 2003).

Although secondary currents akin to those found in river meanders have been observed and modelled in meandering salt-marsh creeks and large estuarine tidal channels (Finotello, Canestrelli, et al., 2019; Finotello et al., 2022; Finotello, Ghinassi, et al., 2020; Kranenburg et al., 2019; Nidzieko et al., 2009; Pein et al., 2018; Somsook et al., 2020; Somsook et al., 2022), their presence in sinuous mudflat channels has yet to be demonstrated. In fact, previous studies (e.g., Choi, 2011; Choi & Jo, 2015; Ghinassi et al., 2019; Kranenburg et al., 2019) suggested that the morphodynamic processes governing meander evolution in intertidal mudflat settings can differ greatly from the classic secondary-current-driven lateral channel migration mechanism acting in vegetated fluvial and intertidal plains. For instance, Kleinhans et al. (2009) argued that owing to the high thresholds for erosion that characterize mudflat deposits, bank erosion is primarily due to bank undercutting caused by backward-migrating steps along the channel bed driven by hydraulic jumps that form during ebb tides. They also demonstrated that bank migration occurs preferentially in very sharp bends, where flow separates from the meander inner (convex) bank and impinges directly against the outer (concave) bank. Choi (2011) noted enhanced tidal channel migration in association with episodic and seasonal increase of discharge due to, for example, heavy precipitations, pointing to a strong control of these non-tidal processes on the morphodynamic and sedimentology of tidal mudflat meanders. Accordingly, Choi and Jo (2015) measured pronounced meander migration in the Yeochari macrotidal flat (South Korea) during the summer rainy season, when point bars were observed to migrate as fast as 40 m per month due to increased runoff discharge caused by heavy rainfalls in the order of tens to hundreds of millimeters per hour, possibly compounded by monsoon precipitations. Finally, Ghinassi et al. (2019) suggested that wave winnowing of mudflats during high-tides modulates meander morphosedimentary evolution, leading to widespread bank collapses into the channel.

In view of the above, the structure of tidal flow fields in mudflat tidal meanders appears to be worth investigating. Here we present novel hydroacoustic data from a meandering tidal channel dissecting a macrotidal mudflat located along the Jiangsu coast (China). The aim of the study is threefold, as we intend to: (i) highlight the characteristics of tidal flows within a meander bend developed in an unvegetated tidal mudflat; (ii) unravel possible differences in meander hydrodynamics among below-bankfull and above-bankfull (i.e., overbank) water stages; and (iii) disclose the characteristics of secondary circulations and their relations with the overbank flows. To the best of our knowledge, this study represents the very first attempt to directly measure tidal flows in meandering mudflat channels.

2 Geomorphological setting and study-case

Our study case is found in the Yangkou tidal flat (YTF), an extensive mud-

flat system located on the southern Jiangsu coast, northward of the Yangtze River Delta, which is bordered by the Yellow Sea to the East and North and by the East China Sea to the South (Figure 2a). The YTF was formed by abundant sediment supply input from both the Yangtze River and the Yellow River, which historically allowed for seaward expansion of the whole Jiangsu province coastline (Shi et al., 2016; Wang & Zhu, 1990). Sediments consist mainly of silty-muddy material, with average grain sizes ranging between 10 and 45 m (i.e., 4.5 ~ 6.6) (Shi et al., 2016; Wang & Ke, 1997). In the last 2 centuries, however, the seaward extent of the YTF has decreased from 5 ~ 11 km to about 5 ~ 8 km as a consequence of changes in sediment transport regime driven by anthropogenic interventions, the latter including the diversion of the Yellow River to the Bohai Sea in 1855 (Ren & Shi, 1986), and the construction of the Three Gorges Dam in 2003, which significantly decreased sediment supply from the Yangtze River (Yang et al., 2014). In addition to this, land reclamation projects, the building of oceanic outfalls, aquaculture, and the construction of wind farms have further contributed to increasing anthropogenic pressures in the YTF area (Xu et al., 2019; Zhao et al., 2020; Zhao & Gao, 2015). Nowadays, the whole intertidal area in the YTF covers approximately 100 km^2, extending seaward from the shoreline with gentle slopes ranging between 0.5‰ and 1.2‰ on average (Wang & Ke, 1997; Zhu et al., 1986).

Intertidal mudflats in the YTF are dissected by extensive networks of tidal channels. These channels serve as the main conduits for the propagation of both the East China Sea progressive tidal wave and the southern Yellow Sea rotary tidal wave, which converge nearby the town of Yangkou giving rise to complex coastal circulations (Liu et al., 1989). The tidal regime in the study area is semidiurnal macro-tidal, with average and spring tidal ranges equal to 4.6 m and 8 m, respectively. Morphodynamic processes are also affected by the East Asian Monsoon, which blows with a mean winter wind speed of 4.2 m/s toward the southeast and a mean summer wind speed of 2.8 m/s toward the northwest, respectively (maximum measured wind speed is 34 m/s; (Li et al., 2011; Xing et al., 2012). As wave conditions of this region are mainly related to wind speeds, wave heights are smaller in the summer and larger in the winter, with annual average values ranging between 0.5 and 1.5 m (Chen, 2016). The annual precipitation is about 900 ~ 1000 mm on average, with the summer season accounting for more than 40% of the whole yearly rainfall (Wang & Ke, 1997; Xing et al., 2012).

Our study site is a blind tidal channel found within a natural reserve facing the Xiaoyaokou Scenic and the Xinchuan port, both located nearby the city of Yangkou (Figure 2b). The studied channel is 1.9 km long and is characterized by average width of 8 m. With an overall channel sinuosity equal to 1.5, it represents a well-developed meandering reach. The channel originates from a fringing salt marsh, which borders the Xiaoyangkou Scenic and is covered by *Spartina alterniflora Loisel* (Figure 2c,e), and extends seaward wandering through an unvegetated intertidal mudflat. Freshwater fluxes from the Beiling river to the North and the Bencha canal to the South do not interfere with the

hydrodynamic regime of the studied channel, which is always submerged at high tide and drains out almost completely at low tide.

In this study, we focused specifically on a meander bend located in the central portion of the channel and surrounded by unvegetated tidal flats (Figure 2c,d,f). The studied bend is characterized by a cartesian wavelength (i.e., the linear distance between bend inflections) L_{xy}=37 m, whereas the along-channel bend length (L_s) is equal to 56 m. Hence, the bend attains a sinuosity χ=L_s/L_{xy}=1.5. The average meander radius of curvature is R=19 m, and the amplitude, measured as the maximum distance from the line passing through both bend inflections, is equal to A=18 m. The cross-sectional width (W) decreases from 8.8 m to 8.3 m in the landward direction (average width $\overline{W}$=8.5 m). Being the bankfull depth (Y_B) equal 1.20 m on average, the studied bend is characterized by an average width-to-depth ratio ($\beta = \overline{W}/Y_B$) of about 7.1. All these morphometric parameters are in line with typical values observed for tidal channels worldwide (D'Alpaos et al., 2005; Finotello, D'Alpaos, et al., 2020; Hughes, 2012). While many regularly-spaced small erosional gullies cut through the channel banks (Figure 2f), a 4 m wide and 0.5 m deep side tributary, meandering in planform, is found landward of the apex of the studied bend (Figure 2d).

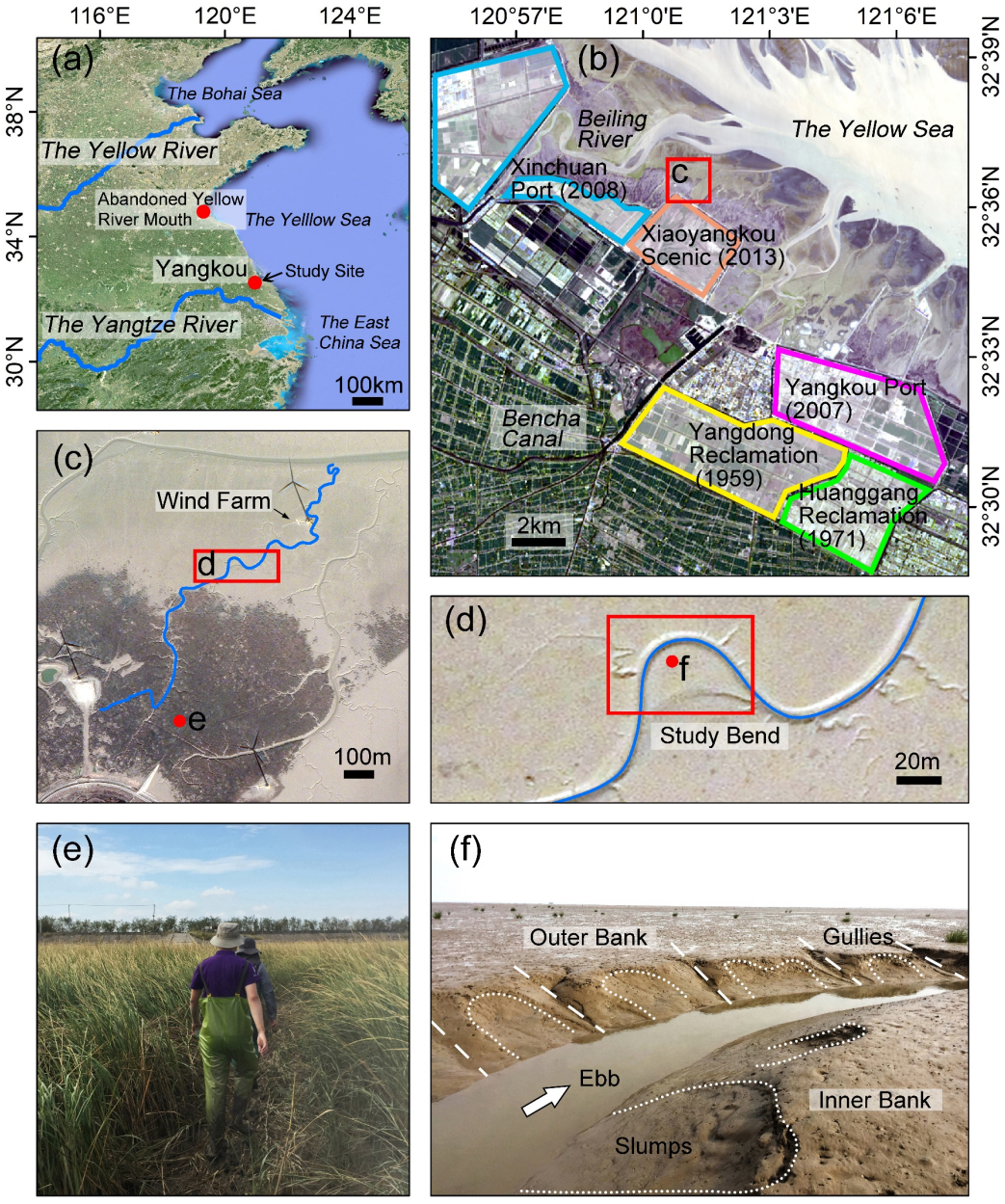

Figure 2. Study site. (a) Overview of the study area. (b) The Yangkou tidal flat, Rudong County, Jiangsu Province, China (Map data: Landsat8, OLI, April 9, 2021); areas affected by land reclamation activities are highlighted with colored lines. (c, d) Overview of the meandering tidal channel investigated in this study, with a close-up view of the analyzed meander bend (Map data: Google, TerraMetrics). (e) A photo showing vegetation features in the landward portion

of the channel, characterized by the widespread presence of *Spartina alterniflora Loisel*. (f) A photo of the studied bend at low tide.

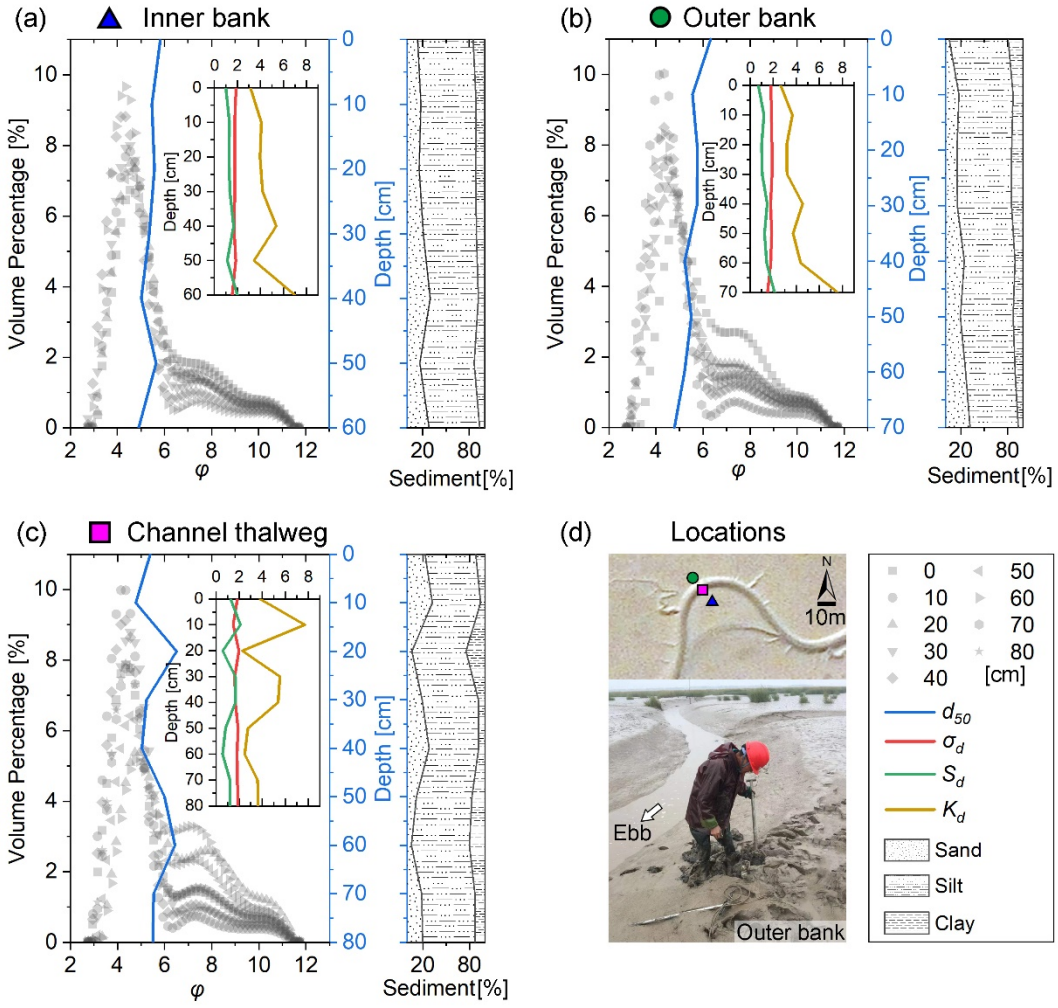

Figure 3. Sediment grain size distribution at the study site. Results of grain size analysis carried out on sediment cores collected at the study-bend inner bank (a), outer bank (b), and channel thalweg (c). Different symbols of gray-shaded data points denote different coring depths, as shown by the inset in the lower-right corner. Detailed coring locations are shown in panel (d), together with a seaward-looking photo of the coring operation at the outer bank. Sediment coring was carried out on the last day of fieldwork to avoid damaging the channel morphology before flow measurements.

In order to investigate sediment properties at the study site, we collected sediment cores at the meander inner bank, outer bank, and channel thalweg using

a custom hand corer (coring depth ranging between 60 and 80 cm). Grain-size analysis was carried out at 10 cm intervals from the core top using a Mastersizer 2000 laser granulometer with a measuring range of 0.02 ~ 2000 m and a reproducibility error of $< 3\%$. Grain-size parameters - including median size (d_{50}), standard deviation (σ_d), skewness (S_d), and kurtosis (K_d) - were calculated using the Moment Methods (Friedman, 1962). Consistently with sedimentary characteristics of the whole YTF system, sediments were found to be mostly cohesive, with clay volume content accounting for nearly 20% (Figure 3). The median grain size is always smaller than 62.5 m (i.e., 4). No significant grain-size trends are observed from the core collected at the channel thalweg (Figure 3c), whereas fining upward trends are found both at the inner and outer bank (Figure 3a,b).

3 Methods

3.1 Acoustic measurements of flow velocities

We continuously monitored water levels and flow velocities in the study meander bend from October 14, 2020 to October 21, 2020. Three Nortek's new Acoustic Doppler Current Profiler (AD2CP, Signature 1000kHz) were placed at three different sites along the studied bend, namely the bend apex and both the landward and seaward inflections, whereas one Teledyne RDI ADCP1200kHz was deployed at the confluence with the small side tributary (Figure 4a). All instruments were placed at the channel thalweg with an up-looking orientation to record velocities and pressures (Figure 4c,d,e,f). The fifth probe of Nortek AD2CPs can observe the vertical velocity separately from the other four probes, thus effectively avoiding acoustic cross-interference so that the noise in the vertical velocity signal is significantly lower than that of traditional ADCP instruments. The three AD2CPs were programmed to operate at 1.0 Hz, recording velocities in 20 cm vertical bins over timespans at 5-minute intervals. The blanking distance of the AD2CP was set to 10 cm, so that the center of the first sampling bin is 20 cm above the instrument. In contrast, the Teledyne ADCP was programmed to operate at 1.0 Hz to record velocities in 5 cm bins at 5 minutes. The blank distance of the ADCP was set to 20 cm, so that the center of the first bin is 22.5 cm above the instrument. Details regarding the instruments' parameters are shown in Table 1.

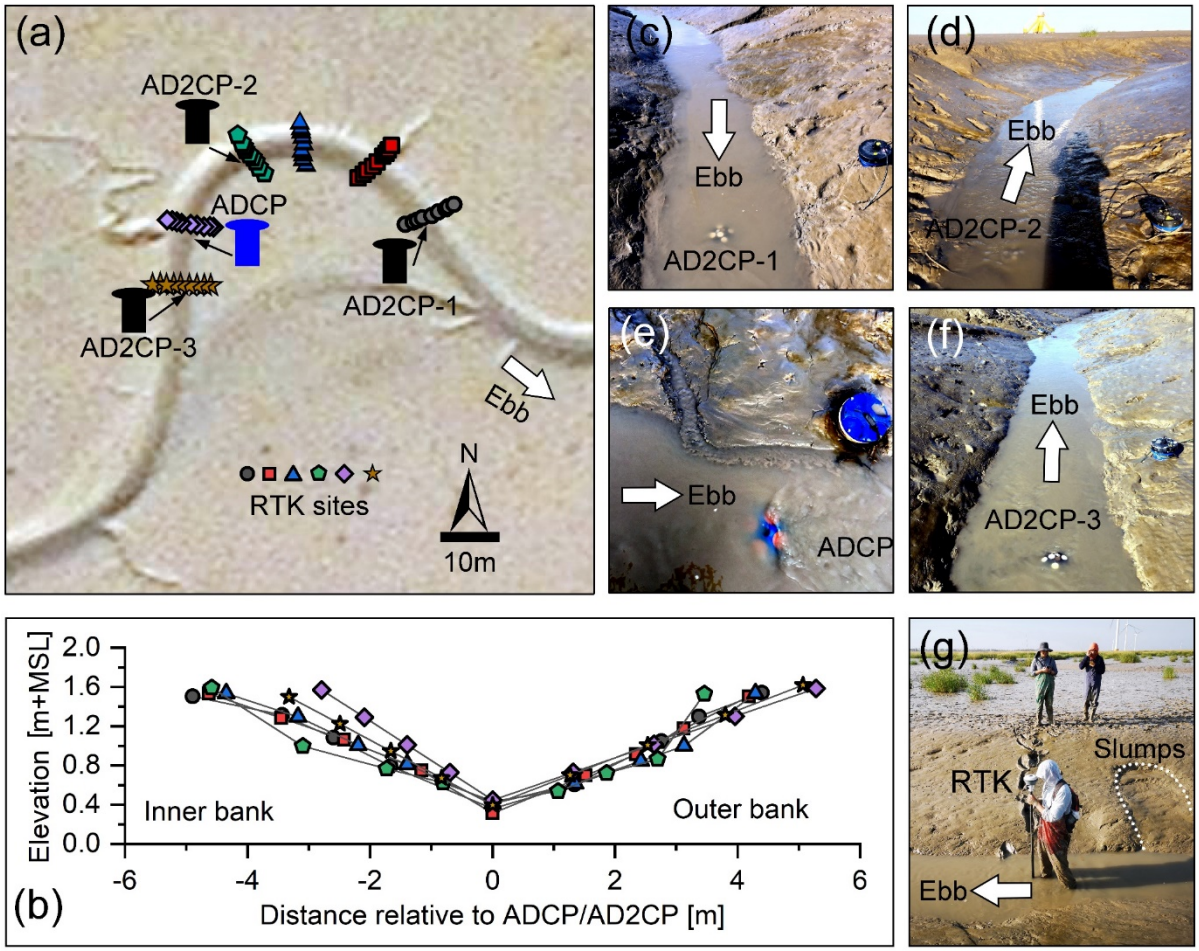

Figure 4. Field measurements of flow fields and channel geometry. (a) Deployment locations of the AD2CPs (in black) and ADCP (in blue) instruments used in this study are shown together with the channel cross-sections where topographic surveys were carried out by means of an RTK-GPS. (b) Cross-sectional profiles of the surveyed channel cross-sections as obtained from the RTK data. Elevations are reported in meters above the mean sea level (MSL). Different symbols and colors denote different cross-sections according to the legend shown in panel "a". (c,d,e,f) Photograph of the deployed instrument prior to data acquisition. Names of individual instruments recall those reported in panel "a". (g) Photo of the topographic survey campaign carried out by means of an RTK-GPS during low tide. All the photos reported in panels c,d,e,f, and g were taken during the late stages of ebb tides.

Table 1. Parameters of the AD2CP and ADCP instruments used in this study

	AD2CP-1	AD2CP-2	AD2CP-3	ADCP
Manufacture	Nortek	Nortek	Nortek	Teledyne RDI
Version	Signature1000	Signature1000	Signature1000	Workhorse
Serial Number	100295	101044	100615	
Sampling rate	1 Hz	1 Hz	1 Hz	1 Hz
Blanking Distance	10 cm	10 cm	10 cm	20 cm
Bin Size	20 cm	20 cm	20 cm	5 cm
Sampling Mode	Burst	Burst	Burst	Burst
Sampling Interval	5 min	5 min	5 min	5 min
Sample Duration	256 s	256 s	256 s	256 s
Burst Profile	5 Beams	5 Beams	5 Beams	4 Beams

3.2 Data processing

Velocity data retrieved from the AD2CPs were converted into ENU system (i.e., v_E, v_N,v_U for East-, North-, and Up-ward velocity, respectively), whereas ADCP data were already recorded in ENU format. Raw ENU data were then imported to Matlab (version 2019b) for initial quality control to remove noise generated by the interference of water bubbles, large suspended particles, echo intensity, and other disturbance factors (Lan et al., 2019). The procedure used for quality control is a modified version of Guerra and Thomson (2017)'s algorithm. For the data acquired using AD2CPs, values of echo intensity 25 dB and correlation magnitude 30% are used as threshold limits for high-quality data; for the data acquired by ADCP, values of echo intensity 30 dB and correlation magnitude 50% are instead used as thresholds. Velocity data were then despiked using the Phase-Space Thresholding Method (Goring & Nikora, 2002) and eventually averaged over the time length of individual burst (i.e., 5 minutes). Moreover, ADCP data were also averaged vertically over 4 successive bins to allow for a more direct comparison with the AD2CP data. Overall, a total of 21 bins of velocity data were obtained for each instrument. For each bin, horizontal velocity $\vec{v}$ was calculated as the vector sum of the eastward ($\overrightarrow{v_E}$) and northward ($\overrightarrow{v_N}$) velocity components (see Figure 5a) whereas depth-averaged velocities ($DAVs$) were computed for each measuring station as the average value of the whole v profile. Measured values of upward velocities ($\overrightarrow{v_U}$) were instead maintained unaltered. Water depth (Y) data were also obtained from pressure sensors integrated within the instruments. Based on the surveyed topographic profile of each cross-section (Figure 4b), we were able to identify the water depth Y_B corresponding to bankfull conditions. This allowed us to differentiate velocity data recorded for water levels higher and lower than the bankfull threshold (i.e., above- and below-bankfull water stages). Stage-velocity diagrams were also obtained based on binary plots of water levels (Y) and depth-averaged values of flow velocity ($DAVs$) at each monitoring station (Figure 6 a-d). Both DAVs and Y were also put in relation to the rates water-level change $\dot{Y} = dY/dt$ (Figure 6 e-h).

Tidal asymmetries were investigated based on two distinct metrics, concerning the asymmetry in flood vs. ebb peak tidal flows and flood vs. ebb durations, respectively (Figure 5 e-g). Asymmetries in tidal duration (ρ_d) were computed as the ratio between the duration of the rising and falling limb of the tidal wave (Friedrichs & Aubrey, 1988; Guo et al., 2019), whereas the ratio (ρ_v) between the flood and the ebb velocity peak of $|\vec{v}|$ (i.e., peak flow asymmetry) over each monitored tidal cycle was used to quantify asymmetries of tidal flow (Friedrichs & Aubrey, 1988; Guo et al., 2019). Both ρ_d and ρ_v provide a straightforward tool to distinguish asymmetric tidal flows into flood-dominated ($\rho > 1$) and ebb-dominated (< 1). To further differentiate between flow dynamics within the channel and outside of it, distinct calculations of ρ_v were performed considering only velocity values measured at water depths (Y) smaller and larger than the bankfull depth (Y_B), respectively (Figure 5e,f).

To simplify the interpretation of velocity-data time series and filter out outliers, data were phase averaged and subdivided into two distinct groups based on the values of the high-tide water depth (Y_H) observed during each individual tidal cycle. Specifically, tidal cycles for which Y_H>3.7 m (i.e., the sixth to thirteenth tidal cycle in Figure 5) were classified as "high-amplitude tides" (HAT), whereas all the other tidal cycles were considered "low amplitude tides" (LAT) (Tu et al., 2019; Voulgaris & Meyers, 2004; Wang et al., 2013). For each tidal cycle, the instant corresponding to Y_H was assigned the time value of t=0. Then, data collected six hours before and after Y_H were ensemble-averaged at five-minute intervals (Figure 7a,b)

Finally, in order to better investigate flow structures and unravel possible secondary (i.e., cross-sectional) circulations, velocity data were reprojected into two different components, namely, the primary (i.e., streamwise) velocity V_P, corresponding to the main direction of in-channel tidal flows, and the secondary (i.e., cross-sectional) velocity V_S, oriented orthogonally to V_P (Bever & MacWilliams, 2016; Finotello, Ghinassi, et al., 2020; Lane et al., 2000). In order to define the directions of V_P and V_S, previous studies have typically taken advantage of reprojection techniques based on flow data recorded along the entire channel cross-section by ADCP instruments mounted on moving vessels (Finotello, Ghinassi, et al., 2020; Lane et al., 2000; Parsons et al., 2013). These techniques cannot however be applied to our data, since our instruments were operated in stationary mode, and significant differences appear when observing flow velocities at above- and below-bankfull stages. Thus, we assumed that the direction of V_P corresponds to the direction of the maximum horizontal velocity ($\overrightarrow{v_{\max}}$) observed at the bottom vertical layer (i.e., Y = 0.2 m in Figure 7c~f). Such a definition is based on the observation that the orientation of $\overrightarrow{v_{\max}}$ at the channel bottom is unequivocally defined and remains consistent during both the ebb and flood phases (see Figure 4 and Figure 7c~f). Once V_P is defined, the orientation of secondary velocity (V_S) is immediately derived as the direction perpendicular to V_P. Details regarding the determination of V_P and V_S at different measuring stations can be seen in Figure 8,9,10 and 11. Close-up views of V_S vectors for below-bankfull stages only are also shown in Supplementary Figure S1.

4 Results

4.1 Flow magnitudes, tidal asymmetries, and stage-velocity relationships

Overbank flows invariably occurred for all the tide cycles on record. The high-tide water depth (Y_H) reached a maximum value of 4.2 m on Oct. 18, whereas a minimum value of Y_H=2.2 m was observed on Oct. 14. The latter was still higher than bankfull water depth (Y_B), which is about Y_B=1.20 m (Figure 5a). There are no significant differences in horizontal velocity magnitudes ($|\vec{v}|$) between the four monitoring stations, with peak velocities in the order of $|\vec{v}|$=0.96-0.99 m/s consistently observed during the rising limb of the tide (Figure 5a,b,c,d). Pronounced differences in flow velocity are observed for water stages above and below the bankfull depth. Specifically, higher $|\vec{v}|$ values are typically observed for below-bankfull water stages, when tidal flows are conveyed entirely within the channel, both during flood and ebb tides. In contrast, comparably lower $|\vec{v}|$ values are found for water levels exceeding the bankfull depth Y_B, although relatively large $|\vec{v}|$ values occur when the high-tide water depth (Y_H) exceeds a critical value of about 3.2 m, that is, for tidal oscillations akin to spring-tide conditions (Figure 5a). When this happens, the vertical velocity profiles display significant variations, with reduced (enhanced) velocities found at water depths lower (higher) than Y_B.

The computed values of tidal flow asymmetries (ρ_v and ρ_d) can be plotted as a function of the high-tide water depth (Y_H) observed during each monitored tidal cycle (Figure 5e,f,g). Made exception for the first monitored tidal cycle, flow velocities are found to be consistently flood-dominated for below-bankfull depths ($Y<Y_B$, Figure 5e). In contrast, ebb dominance becomes more common considering water depths above the bankfull ($Y>Y_B$), even though most of the data still falls within the flood-dominated domain (Figure 5f). Changes in high-tide water depth (Y_H) seem to not significantly affect peak flow asymmetry, although both data scattering and flood dominance appear to decrease slightly as Y_H increases, both for above- and below-bankfull water depths (Figure 5e,f). Conversely, variations in Y_H significantly affect tide duration asymmetry (ρ_d). The collected data suggest the persistence of flood-dominated conditions in our study channel during the entire monitoring period, with ρ_d increasing proportionally to Y_H in a statistically significant fashion (Figure 5g).

Stage-velocity diagrams for all the measuring stations display pronounced variations in the observed depth-averaged velocity (DAV), with DAV maxima typically occurring immediately below the bankfull water depth both for flood and ebb tides (Figure 6a,b,c,d). Flood *DAVs* are observed to decrease significantly once water depths exceed the bankfull stage. On the contrary, ebb *DAVs* rapidly increase once water depths become lower than the bankfull water depth. Although the peak *DAVs* are typically higher during the flood phase, which is in agreement with our previous observations regarding flow asymmetries, ebb *DAVs* attain near-maximum values for comparably longer times at water stages lower than bankfull (Figure 6a,b,c,d).

Similar to the DAV patterns, the rate of water-level change ($\dot{Y} = dY/dt$) peaks around the bankfull stage during the flood, whereas ebb peaks of $\dot{Y}$ are observed for water stages well above the bankfull (Figure 6e,f,g,h). Notably though, $\dot{Y}$ attains a nearly-constant value during most of the ebb phase, whereas much more pronounced changes are observed during the flood. A statistically significant, positive linear correlation is found between $\dot{Y}$ and DAV for below-bankfull stages during both the ebb and the flood (Figure 6i,j,k,l), although such correlation is more robust for ebb flows (Figure 6i,j,k,l). For overbank stages, significant correlations between $\dot{Y}$ and DAV can only be obtained for the flood phase, whereas ebb $DAVs$ are not significantly correlated to $\dot{Y}$ (Figure 6m,n,o,p).

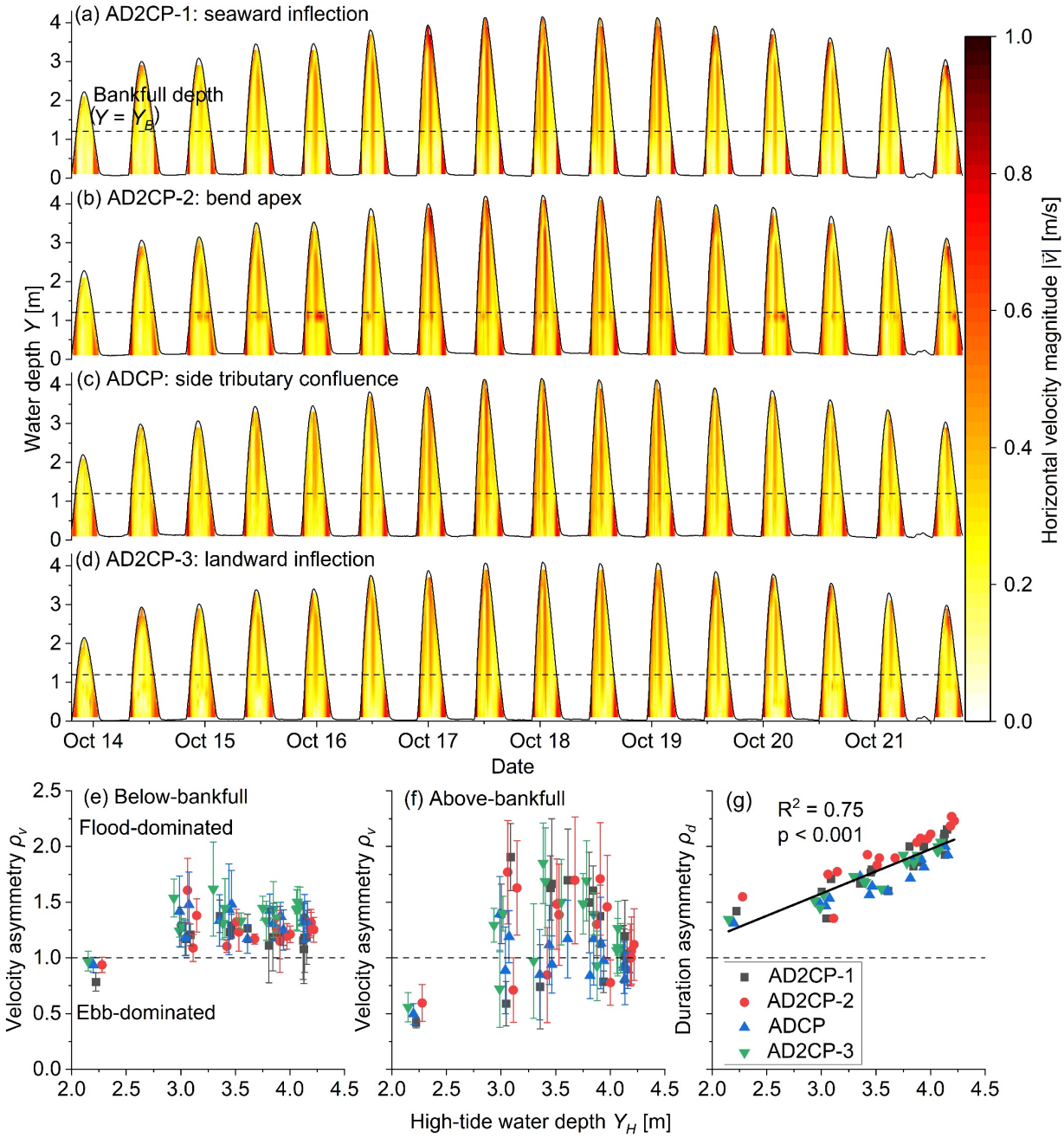

Figure 5. Time series of measured flow velocities and water depths. a,b,c,d) Time-continuous plots of horizontal velocity magnitudes ($|\vec{v}|$) as a function of instantaneous water depth (Y) for AD2CP-1 (seaward inflection point, panel a), AD2CP-2 (bend apex, panel b), ADCP (confluence with side tributary, panel c),

and AD2CP-3 (landward inflection point, panel d). The horizontal velocity magnitude is computed as $|\vec{v}| = \sqrt[2]{|\overrightarrow{v_E}|^2 + |\overrightarrow{v_N}|^2}$, where $\overrightarrow{v_E}$ and $\overrightarrow{v_N}$ are the Eastward and Northward velocity components measured by the acoustic instruments, respectively. The horizontal, black-dashed line in each panel denotes water depth corresponding to the bankfull stage (Y=Y_B) for each measuring station. (e,f) Values of peak tidal velocity asymmetry (ρ_v) at different measuring stations are plotted against the high-tide water depth (Y_H) observed during each monitored tidal cycle. Panel e) shows ρ_v for below-bankfull tidal flows, whereas ρ_v values for above-bankfull flows are displayed in panel f). Data points represent the average value of ρ_v computed at different depths, with error bars denoting standard deviation. (g) Values of tidal duration asymmetry (ρ_d) at different measuring stations are plotted against the high-tide water depth (Y_H) observed during each monitored tidal cycle. Different symbols and colors in panels e,f, and g denote different monitoring stations according to the legend in the lower-right inset. Calculations of tidal asymmetries were carried out only when instruments were submerged and both velocity and depth data could effectively be recorded.

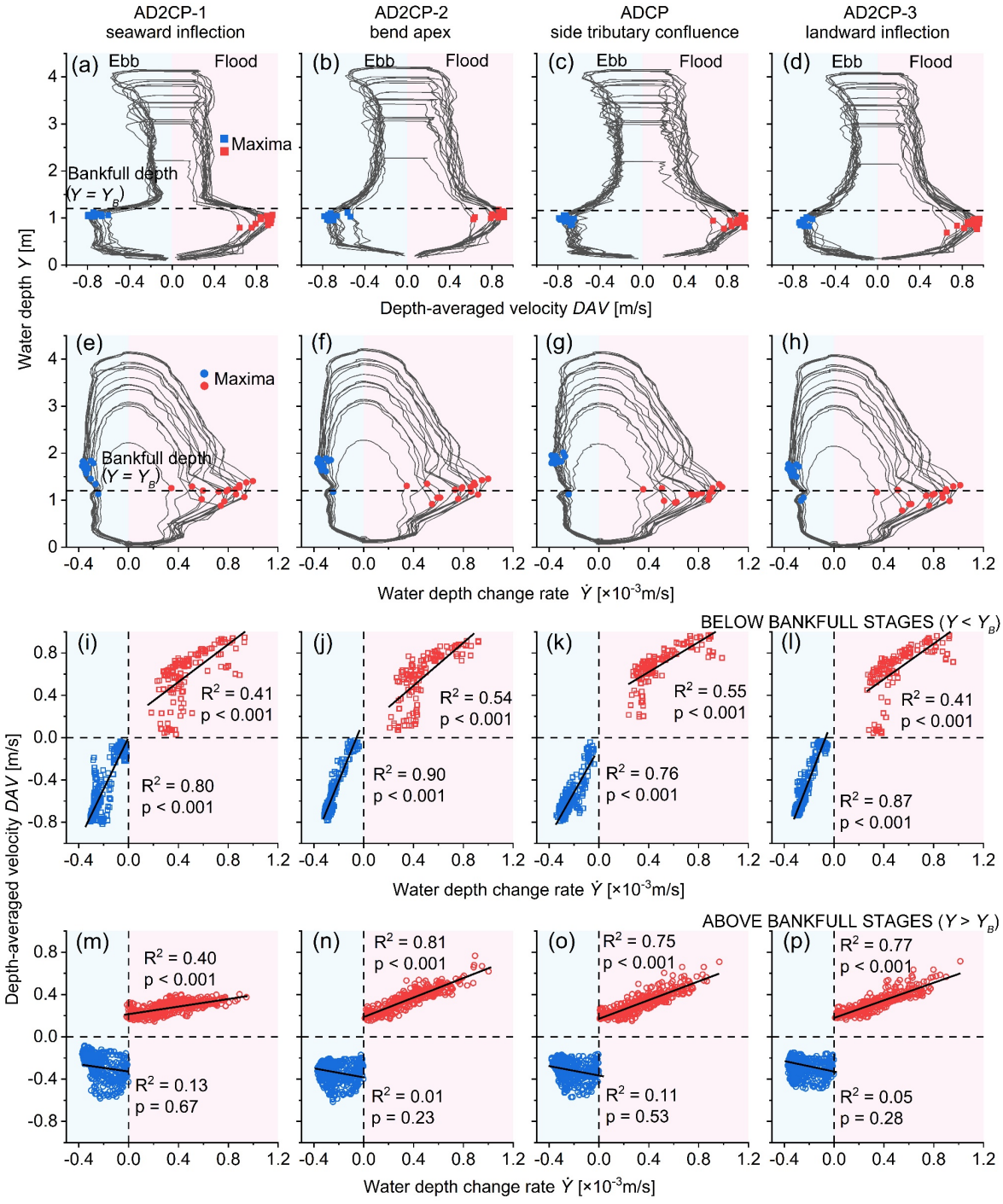

Figure 6. Relationships between depth-averaged velocity (DAV), water depth

(Y), and water-depth change rate ($\dot{Y} = dY/dt$) at the four measuring stations. Columns from the left- to the right-hand side of the figure show, respectively, results for AD2CP-1 (seaward inflection point), AD2CP-2 (bend apex), ADCP (side tributary confluence), and AD2CP-3 (landward inflection point). Red and blue quadrants represent data obtained during the flood and the ebb phase, respectively. (a, b, c, d) Water depth (Y) vs. depth-averaged velocity (DAV) curves for all the monitored tidal cycles. Red and blue points denote the maximum flood and ebb *DAVs* of each tidal cycle. (e, f, g, h) Water depth (Y) vs. water-depth change rate ($\dot{Y}$) curves for all the monitored tidal cycles. Red and blue points denote the maximum flood and ebb $\dot{Y}$ of each tidal cycle. (i, j, k, l) Depth-averaged velocity (DAV) as a function of water-depth change rate ($\dot{Y}$) for below-bankfull stages during all the monitored tidal cycles. (m, n, o, p) Depth-averaged velocity (DAV) as a function of water-depth change rate ($\dot{Y}$) for above-bankfull stages during all the monitored tidal cycles.

4.2 Phase averaged velocities and secondary circulations

4.2.1 Horizontal flow velocities

Horizontal flow vectors $\vec{v}$ at different depths are plotted for high-amplitude (HAT) and low-amplitude (LAT) cycles separately (Figure 7c~f). At each measuring station, ebb and flood $\vec{v}$ for below-bankfull stages are generally characterized by similar orientations, yet with opposite directions, whereas more scattering is observed when flow depth exceeds the overbank stage. Directions of overbank flows appear to be consistent across different measuring stations, with flood and ebb flows directed to the southwest and southeast, respectively. In contrast, inter-site variability of below-bankfull flows is more marked, as $\vec{v}$ appears to follow the orientation of the channel axis, with $\vec{v}$ being more variable and generally less correlated to the channel axis orientation for near-bankfull conditions (i.e., water depths $0.8<Y<1.2$m). It is also worthwhile noting that flow directions at any given measuring station display little differences between HAT and LAT cycles, both for water stages above and below the bankfull.

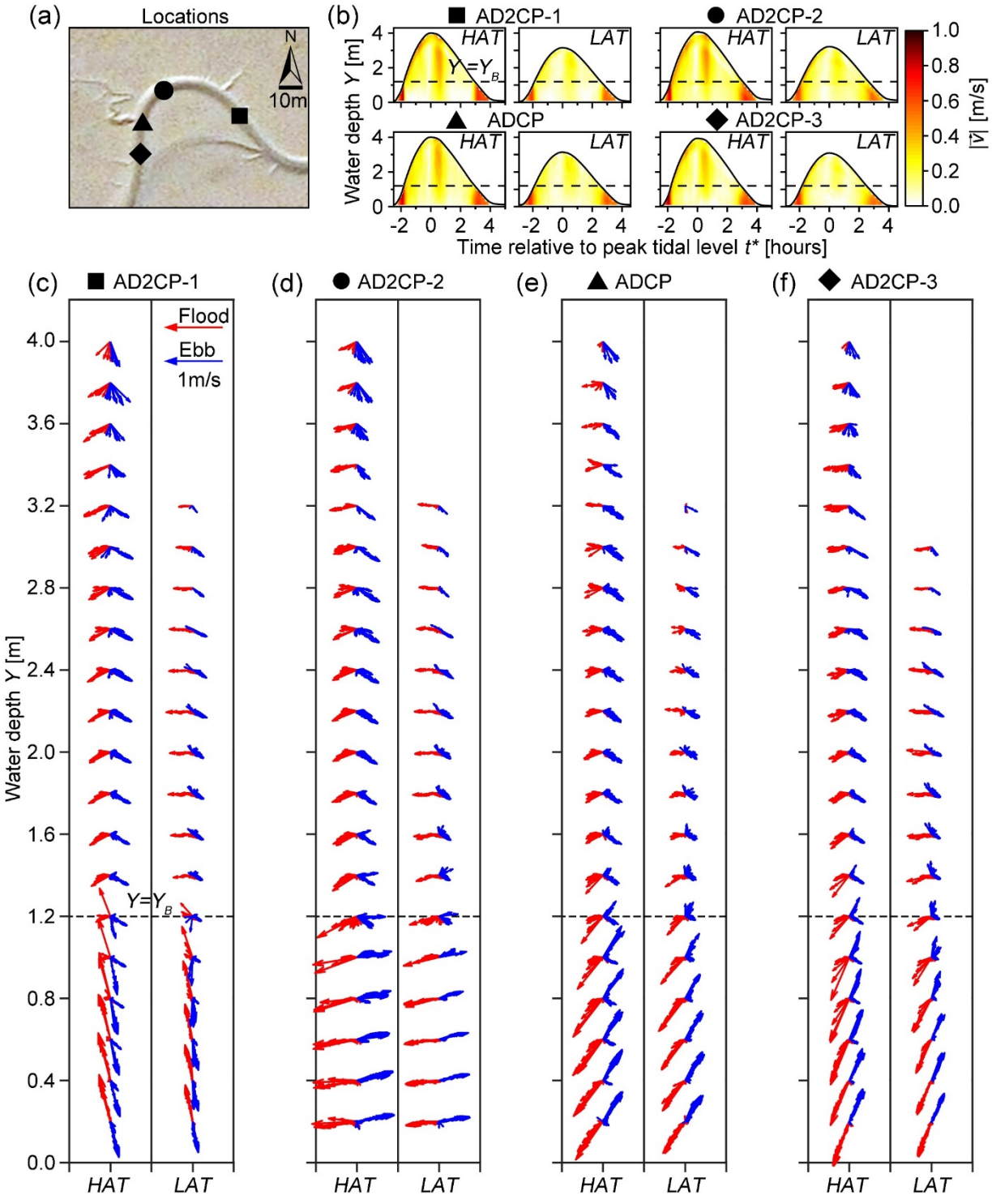
(a)
Locations
N
10m
(b)
AD2CP-1
AD2CP-2
ADCP
AD2CP-3
HAT
LAT
Y=Y_B
Water depth Y [m]
|V| [m/s]
Time relative to peak tidal level t* [hours]
(c)
(d)
(e)
(f)
Flood
Ebb
1m/s
Water depth Y [m]

Figure 7. Ensemble phase-averaged horizontal velocity ($\vec{v}$) data at the four measuring stations. (a) Locations of measuring stations. (b) Time series of $\vec{v}$ magnitudes computed separately for high-amplitude tides (HAT) and low-amplitude tides (LAT) at each measuring station. (c,d,e,f). Vectors of horizontal velocities in HAT and LAT cycles plotted for different water depths (Y) at each measuring station during the ebb (blue) and flood (red).

4.2.2 Streamwise velocities and secondary circulations

In all the measuring sites, the primary (i.e., streamwise) velocity (V_P) reduces significantly once the water stage reaches bankfull, both for HAT and LAT cycle. On the contrary, V_S increases significantly once water depth exceeds the bankfull (see panel b in Figures 8,9,10, and 11). To better describe flow dynamics near the bankfull stage, we also plot V_S vectors overimposed to V_P magnitude values computed 15 minutes before and after the bankfull stage for both HAT and LAT cycle (see panel c~f in Figures 8,9,10, and 11).

Velocity patterns observed at the seaward inflection site (AD2CP-1) are reported in Figure 8c~f. During the flood, once the water depth exceeds the bankfull, V_P decreases suddenly and even reverses its direction in the upper layers, where V_S increases significantly and takes direction pointing toward the meander inner bank. In contrast, during the ebb, V_S is very weak both for the above- and below-bankfull stages (Figure 8c~f).

Similar results are observed at the landward inflection site (Figure 9). Particularly, peaks in V_P are observed for $Y<Y_B$, whereas the largest values of V_S are attained when water depths exceed the bankfull ($Y>Y_B$). During the flood, secondary velocities (V_S) are generally higher than at the seaward inflection and consistently point to the outer bank in the upper vertical layers. Possible secondary circulations emerge during the flood for both HAT and LAT cycles, with V_S directed toward the outer bank at the water surface and near the inner bank at the channel bottom. Overall, data from both the landward and seaward inflection sites suggest the presence of secondary circulations for overbank stages both for HAT and LAT cycles, with less obvious patterns being observed during below-bankfull stages (Figure 8,9; see also Supplementary Figure S1a,b).

Secondary circulations can be observed at the bend apex (Figure 10), though they appear to be generally weaker than those found at the bend inflections. During the flood, both V_S magnitude and secondary circulations are very weak when $Y<Y_B$ (Figure 10b~f and Figure S1c). Once Y reaches Y_B, V_S increases and secondary circulations develop, especially during HAT cycles. However, contrary to classic (i.e., fluvial) secondary circulation patterns where flows are directed toward the outer bank in the uppermost portions of the water column, we observe secondary circulations characterized by V_S directed toward the inner bank near the water surface. During ebb tides, V_S are generally lower than during the flood, and secondary circulations are less clearly noticeable both for HAT and LAT cycles.

Finally, at the confluence site, no significant secondary circulation is detected

during either the flood or the ebb, both for *HAT* and *LAT* cycles. During the flood, V_S are consistently directed toward the outer bank where the tributary is located and increase significantly when the water rises above the bankfull stage (Figure 11b~f; see also Supplementary Figure S1d). In contrast, during the ebb, a chaotic distribution of V_S is found, with no clear indication of relevant secondary circulations (Figure 11d,f, Figure S1d).

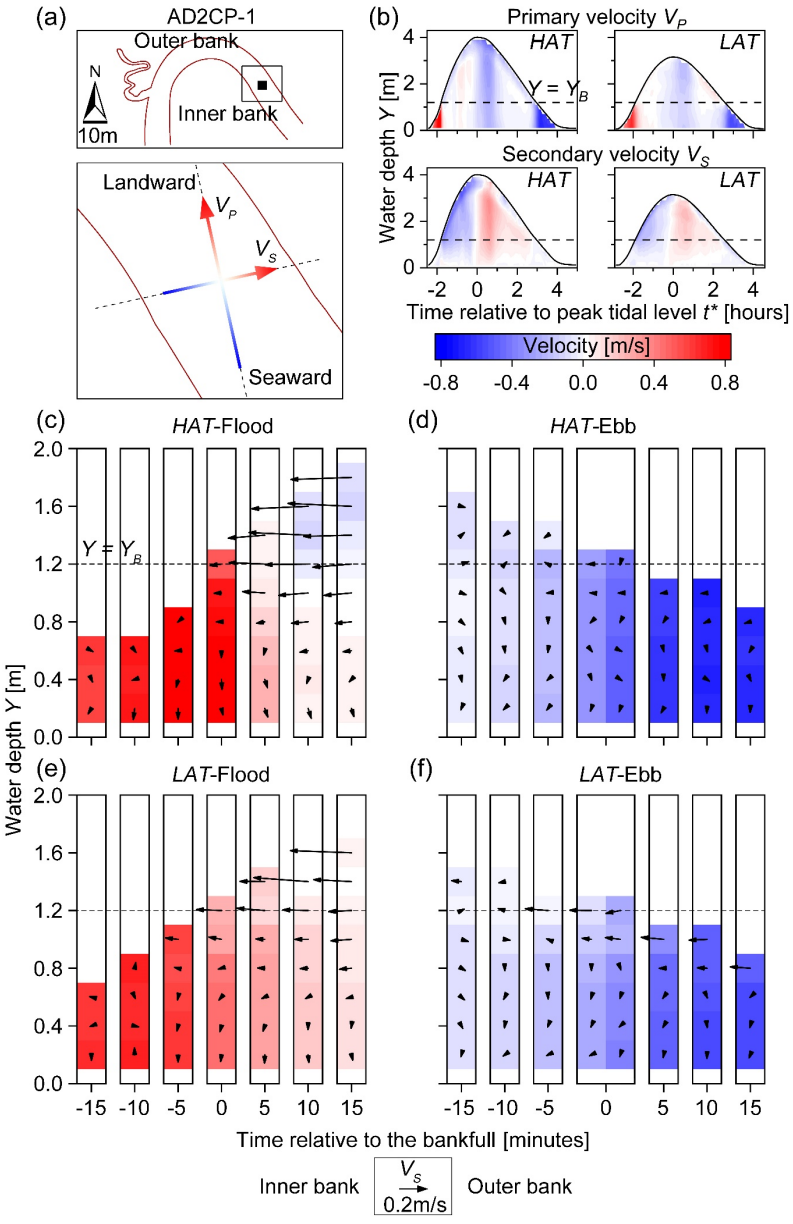

Figure 8. Flow decomposition at the seaward inflection site. (a) Location of AD2CP-1 and the direction of primary (V_P) and secondary velocity (V_S). (b) Time series of V_P and V_S during high-amplitude tide (HAT) and Low-amplitude tide (LAT). (c,d,e,f) Vertical distribution of V_P magnitude with overimposed V_S vectors computed, at 5-minute intervals, 15 minutes before and after the bankfull stage in the HAT and LAT cycle. V_s are directed toward the inner and outer bank when pointing to the left- and right-hand sides of the figure, respectively.

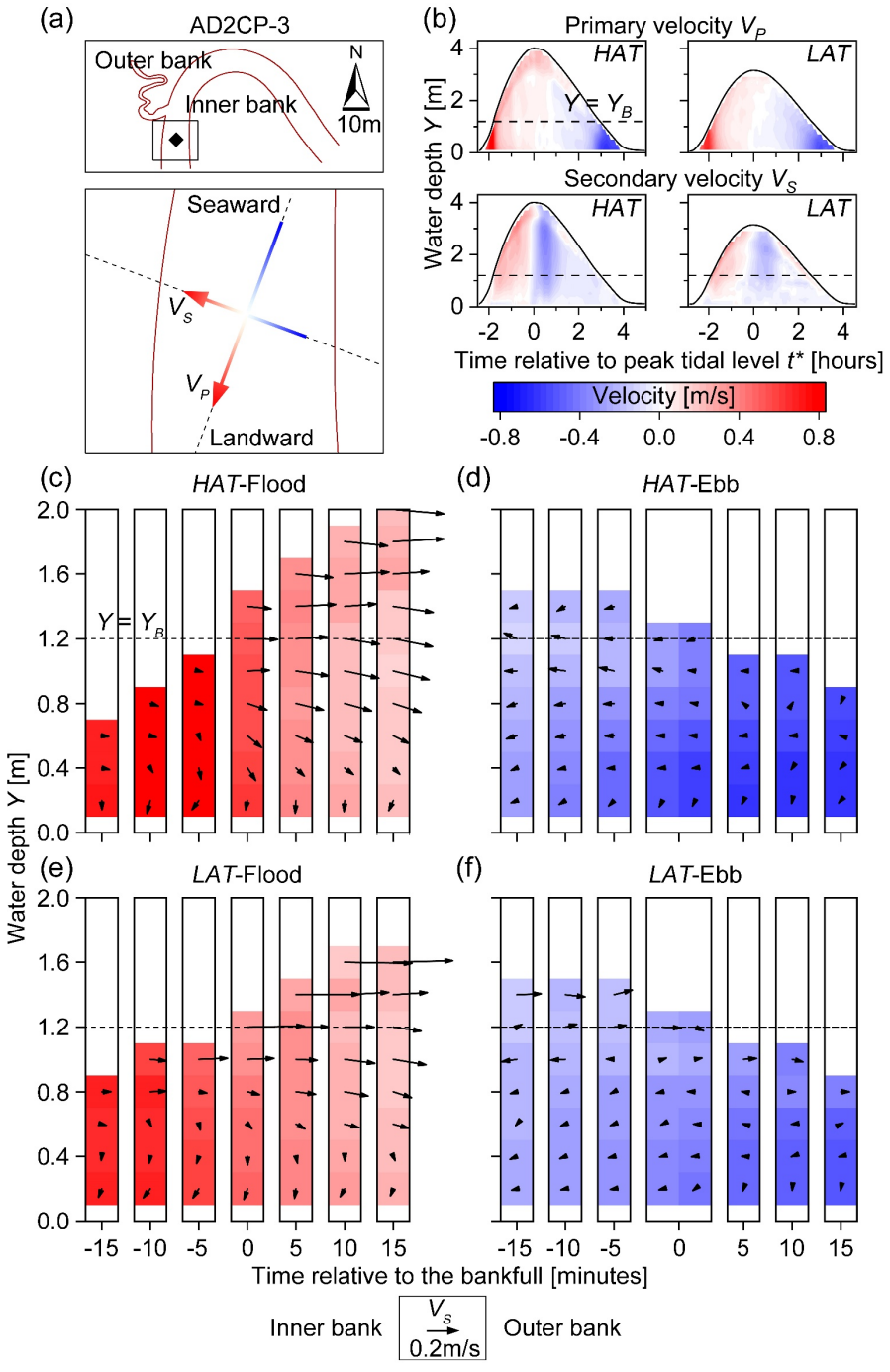

Figure 9. Flow decomposition at the landward inflection site. (a) Location of AD2CP-3 and the direction of primary (V_P) and secondary velocity (V_S). (b)

Time series of V_P and V_S during high-amplitude tide (HAT) and Low-amplitude tide (LAT). (c,d,e,f) Vertical distribution of V_P magnitude with overimposed V_S vectors computed, at 5-minute intervals, 15 minutes before and after the bankfull stage in the HAT and LAT cycle. V_s are directed toward the inner and outer bank when pointing to the left- and right-hand sides of the figure, respectively.

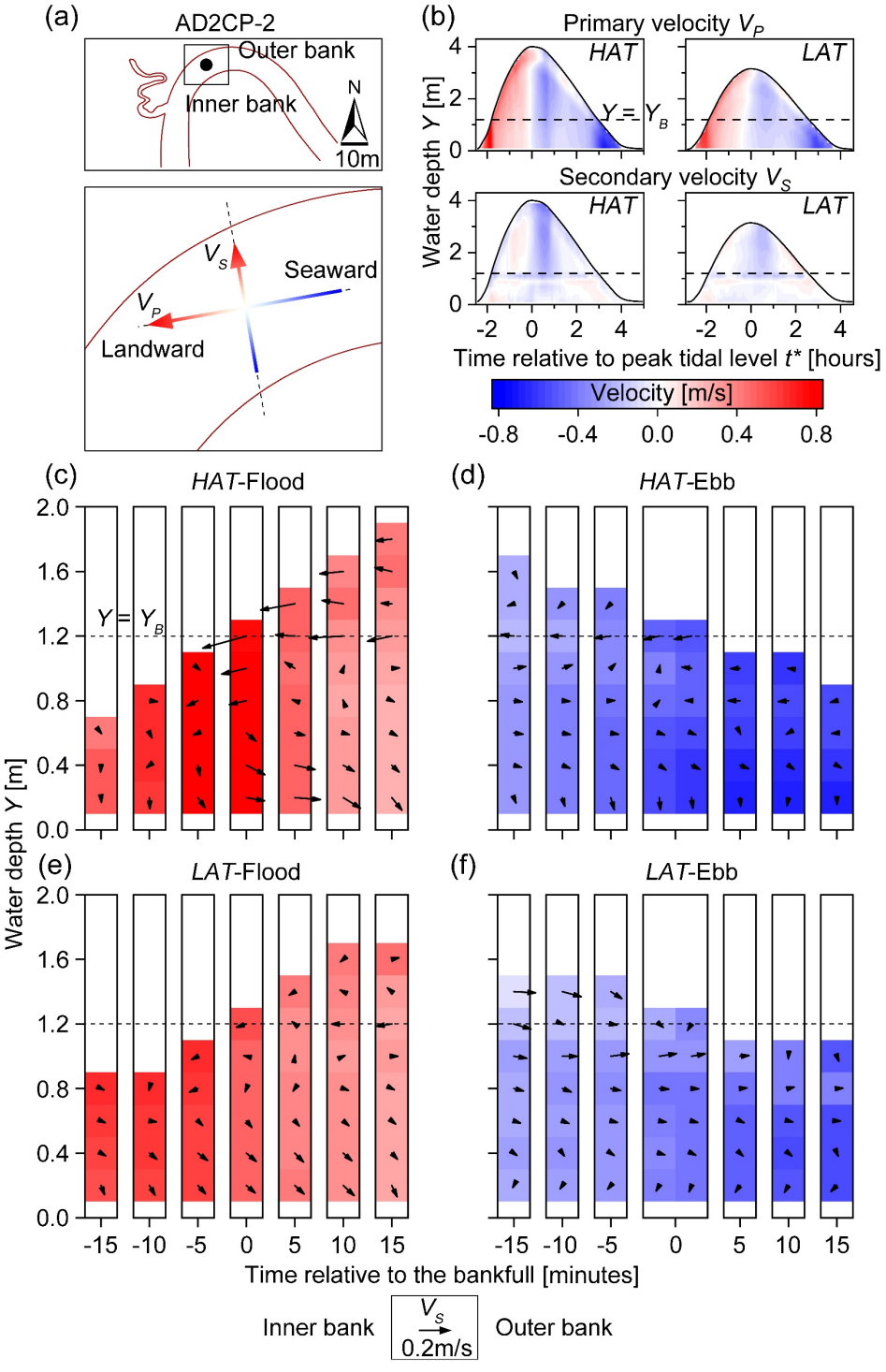
(a)
AD2CP-2
Outer bank
Inner bank
N
10m
V_S
Seaward
V_P
Landward
(b)
Primary velocity V_P
HAT
LAT
$Y = Y_B$
Secondary velocity V_S
Water depth Y [m]
Time relative to peak tidal level t^* [hours]
Velocity [m/s]
-0.8 -0.4 0.0 0.4 0.8
(c)
HAT-Flood
(d)
HAT-Ebb
(e)
LAT-Flood
(f)
LAT-Ebb
Time relative to the bankfull [minutes]
Inner bank
V_S
0.2m/s
Outer bank

Figure 10. Flow decomposition at the apex site. (a) Location of AD2CP-2 and the direction of primary (V_P) and secondary velocity (V_S). (b) Time series of V_P and V_S during high-amplitude tide (HAT) and Low-amplitude tide (LAT). (c,d,e,f) Vertical distribution of V_P magnitude with overimposed V_S vectors computed, at 5-minute intervals, 15 minutes before and after the bankfull stage in the HAT and LAT cycle. V_s are directed toward the inner and outer bank when pointing to the left- and right-hand sides of the figure, respectively.

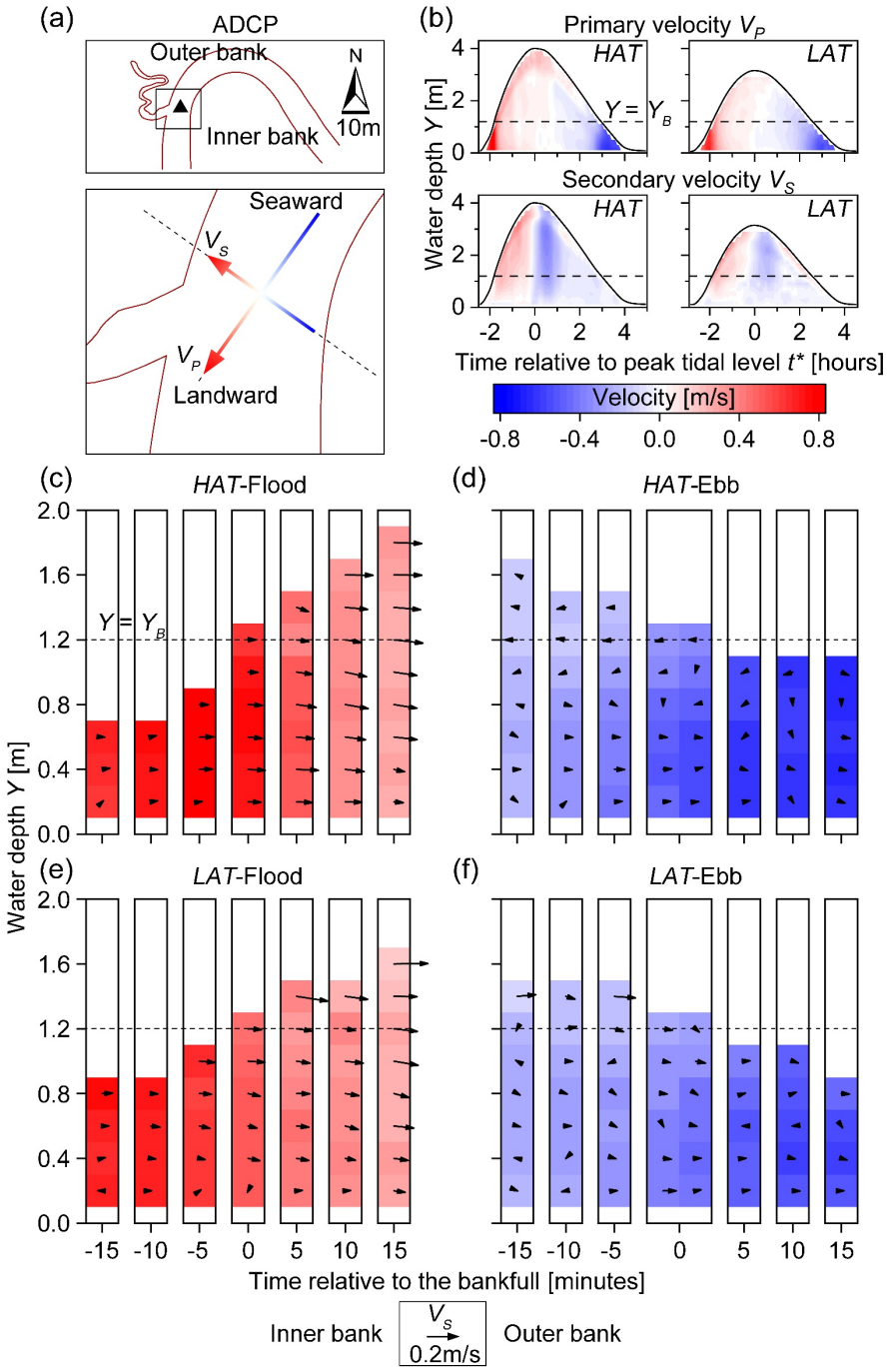

Figure 11. Flow decomposition at the confluence site. (a) Location of ADCP and the direction of primary (V_P) and secondary velocity (V_S). (b) Time se-

ries of V_P and V_S during high-amplitude tide (HAT) and Low-amplitude tide (LAT). (c,d,e,f) Vertical distribution of V_P magnitude with overimposed V_S vectors computed, at 5-minute intervals, 15 minutes before and after the bankfull stage in the HAT and LAT cycle. V_s are directed toward the inner and outer bank when pointing to the left- and right-hand sides of the figure, respectively.

5 Discussions

5.1 Overbank flows and stage-velocity relationships

Horizontal velocity distributions and stage-velocity diagrams of our studied channel display critical differences compared to those observed in channels wandering through vegetated salt marshes and mangrove forests (D'Alpaos et al., 2021; Fagherazzi et al., 2008; Hughes, 2012; Kearney et al., 2017; McLachlan et al., 2020; van Maanen et al., 2015; see Figures 5 and 6). Owing to the characteristic geomorphic structure of vegetated intertidal plains, peaks of ebb and flood velocities in tidal channels typically occur just below or above the bankfull stage (i.e., for $Y>Y_B$), with velocities being significantly reduced at $Y<Y_B$ and approaching null values when Y is minimum (see Bayliss-Smith et al., 1979; Boon, 1975; Fagherazzi et al., 2008; Hughes, 2012; Kearney et al., 2017). In contrast, our monitored mudflat channel is characterized by sustained velocities at $Y<Y_B$, with both horizontal ($\vec{v}$) and depth-averaged velocities (DAVs) peaks occurring when tidal flows are confined within the channel banks (Figures 5 and 6). Notably, in all the monitored sites velocities are relevant (DAV 0.8 m/s) even for reduced water depth ($Y<0.5$ m), especially during the ebb (see Figure 6a,b,c,d). Overbank stages are instead characterized by reduced velocities, both in terms of $\vec{v}$ and DAV values (Figures 5 and 6).

These discrepancies in velocities fields between channels found in vegetated and unvegetated intertidal settings are likely due to the relative speed at which tides can propagate within and outside tidal channel networks. Specifically, frictionally-dominated tidal flows across vegetated intertidal plains make channels preferential pathways for tide propagation even when water levels exceed the bankfull (i.e., for $Y>Y_B$; D'Alpaos et al., 2007; Rinaldo et al., 1999a, 1999b). In contrast, flow resistance in unvegetated mudflats is comparable between tidal channels and intertidal plains, such that tide propagation through unvegetated intertidal mudflats is dominated by sheet flow. This hypothesis is supported by field data from the meso-macrotidal Scheldt Estuary (Vandenbruwaene et al., 2015) highlighting similar velocities within tidal channels (0.3~1 m/s) and across bare intertidal mudflats (0.1~0.4 m/s), in contrast to salt marshes wherein tidal flow velocities are typically lower than 0.1 m/s. In our studied channel, flow velocities for above- and below-bankfull stages are found to be in the range 0.2~0.4 m/s and 0.2~1 m/s, respectively (Figure 5,6), which roughly correspond with the results of Vandenbruwaene et al. (2015). The latter data also suggest that instantaneous water levels are not significantly different within channels and across mudflats, in contrast to frictionally-dominated vegetated intertidal plains where significant differences in instantaneous water levels occur moving away from tidal channels (D'Alpaos et al., 2021; Rinaldo et al., 1999a, 1999b;

Sullivan et al., 2015).

Besides differences in bottom friction at overbank stages, one should also appreciate that hydrodynamic dissimilarities are to be expected in mudflat vs. salt-marsh channels as a consequence of distinct characteristic elevations of both their banks and the adjoining intertidal platforms. Mudflat channels typically occupy the lower portions of the intertidal frame, their bank elevation typically ranging between the mean sea level (MSL) and the mean low water springs (MLWS). This allows for significant water depths at above-bankfull stages, which reduce flow confinement within the channel and limit channel flow velocities (Brooks et al., 2021). In contrast, channel banks in salt marshes are typically located in the highest portions of the intertidal frame, which ensures in-channel flow confinement and sustained flow velocities even for large tidal oscillations, effectively limiting above-bankfull water depths. In our study case, high $\vec{v}$ during overbank stages are only observed when peak tidal levels exceed $Y_{\max}$>3.2 m, that is, for spring tidal cycles (Figure 4a,b,c,d) or, more generally, for high-amplitude (*HAT*) tidal cycles (Figure 7b). Such high $\vec{v}$ values are however likely related to overbank circulations occurring at the scale of the entire mudflat systems, which are not necessarily related to flow dynamics within the channel. This is confirmed by the analysis of $\vec{v}$ directions along the water column (Figure 7c), which testifies clear deviations of tidal flows at $Y>Y_B$ relative to the orientation of the channel axis both for *HAT* and *LAT* tidal cycles. Such a deviation produces consistent flow directions in all the monitored sites, with tidal flows being directed to the South-East and South-West during ebb and flood tides, respectively (Figure 7c).

These observations altogether support the idea that differences in the character of overbank flows result in marked hydrodynamic dissimilarities between tidal channels dissecting vegetated and unvegetated intertidal plains. Such differences are also likely to affect curvature-induced secondary circulations and the related meander morphodynamic evolution, as we discuss in detail in the next sections.

5.2 Secondary circulations and curvature-induced helical flows

According to classic flow fields observed in sinuous channels, secondary (i.e., cross-sectional) circulations are observed in our study bend, both during high-amplitude (*HAT)* and low-amplitude (*LAT*) tidal cycles (Figures 8,9,10,11). These secondary circulations are more pronounced during overbank stages, their intensity increasing as the water depth increases within the studied channel. Indeed, secondary circulations tend to be stronger for *HAT* than *LAT* cycles (Figures 8,9,10,11). They also appear to be mostly related to flood flows, which is in agreement with the generally flood-dominated character of tidal flows observed in the studied bend (Figure 5e,f,g). In some cases, the orientation of secondary circulations is reversed compared to classic flow models such as, for example, at the seaward bend inflection as well as at the meander apex (Figure 8 and Figure 10), where secondary circulations are directed toward the inner and outer bank at the top and bottom of the water column, respectively. Secondary currents can trigger cross-sectional sediment transport processes such

that fine-grained deposits are transported up to the point bar from the channel bed, giving rise to fining upward trends due to the progressive upbar weakening of secondary currents (Bathurst et al., 1977; Blanckaert, 2011; Dietrich, 1987; Termini & Piraino, 2011). This is supported by the fining upward trends that are consistently observed from sediment cores collected at different sites along the studied bend (Figure 3).

Interestingly, secondary circulations are more pronounced at the meander inflections than at the apex, where they should be stronger owing to higher channel curvature. This could however depend on the surveying strategy we used, since we only monitored the velocity profile in correspondence to the channel axis rather than across the entire cross-section. Previous studies have demonstrated that secondary circulation cells do not necessarily occupy the whole channel cross-section (e.g., Blanckaert, 2009, 2011; Finotello, Ghinassi, et al., 2020). Particularly, hydrodynamic nonlinearities can arise in sharp bends characterized by radius-to-width ratios $R/\overline{W}$ lower than 2-3, and flow separation may occur either at the inner or outer bank, respectively, immediately upstream or downstream of the bend apex (Blanckaert et al., 2013; Finotello, Ghinassi, et al., 2020; Hickin, 1978; Hickin & Nanson, 1975; Hooke, 2013; Parsons et al., 2004; Rozovskiĭ, 1957). Flow separation, which is common in tidal meanders owing to the high curvature values that they typically display (Ferguson et al., 2003; Finotello, D'Alpaos, et al., 2019), can effectively reduce the portion of the channel that is hydrodynamically active and confine curvature-induced secondary circulations to the nonrecirculating portion of the primary flow (Finotello, Ghinassi, et al., 2020; Leeder & Bridges, 1975; Parsons et al., 2004). Our studied meander bend is characterized by a $R/\overline{W}$=2.2, and the formation of flow sepeartion is therefore highly likely. Direct measurement of tidal flows across the entire channel cross section would be necessary to settle the dispute, but such data are hard to collect because channel banks at our studied site are flooded by more than 3 m of water at high tides, thus making field measuring campaigns complicated. Nevertheless, we can still estimate the chance for flow separation at the apex of our studied channel by comparing our data with the results obtained by Leeder and Bridges (1975) for intertidal meanders in the vegetated Solway Firth (Scotland). According to Leeder and Bridges (1975), the chances for flow separation in tidal meander bends can be expressed as a function of bend tightness ($\frac{R}{W}$) and Froude number (Fr). Although extending the results of Leeder and Bridges (1975) to unvegetated mudflats might not be entirely appropriate, results would still offer useful insights on the possible occurrence of flow separation, especially for below-bankfull stages when tidal flows are confined within the channel. Since our measurements include several consecutive tidal cycles, we were able to calculate how the $\frac{R}{W}$ changes according to varying water depths. Specifically, we assumed that R does not vary significantly with changing water elevation, and we computed the channel width W_Y corresponding to different water depths (Y) based on topographic data of the meander-apex cross-section (Figure 4b). Plotting of $\frac{R}{W_Y}$ against Fr shows that flow separations at the bend apex site are likely to occur at near-bankfull stages (Figure 12). This

is clearly related to the morphology of the studied bend, which is characterized by a relatively low width-to-depth ratio (β), whereby W_Y increases rapidly as Y increases, thus producing progressively lower $\frac{R}{W_Y}$ in the range from 8 to 2. In addition, flow velocities at the below-bankfull stage generate a modest Fr value of 0.2~0.3, which can possibly induce flow separations (Leeder & Bridges, 1975). In contrast to our observations, Figure 12 suggests that flow separation will be suppressed at overbank stages, likely because of the observed flow velocity reduction at $Y>Y_B$. Care should be however given when extending the results proposed by Leeder and Bridges (1975) to situations where tidal flows do not remain confined within channel banks. Regardless, our analyses support the idea that reduce secondary circulations observed at the meander apex could be ascribed to flow separation, which makes secondary circulations hard to identify through localized flow measurements.

Regardless of flow separation, it is worthwhile noting that secondary circulations are stronger during overbank stages, when flow confinement within channel banks is significantly reduced and, as a result, primary velocities (V_P) are small. Thus, there seems to be a phase shift between peaks of primary (V_P) and secondary velocity (V_S), such that V_P is maximum when V_S is low, and vice versa. Such a shift would effectively limit the advection of cross-stream circulations operated by the primary flow, thus hampering the formation of characteristic curvature-induced helical flows (e.g., Blanckaert, 2011; Blanckaert & de Vriend, 2003; Dinehart & Burau, 2005; Ferguson et al., 2003; Frothingham & Rhoads, 2003). Moreover, we notice that primary velocities at overbank stages are sometimes characterized by reverse direction relative to below-bankfull stages, that is, V_P are directed seaward (landward) during flood (ebb) tides (see for example Figure 8c). This would further limit the transfer of secondary circulation by primary velocity along the meander bend, thus hampering the formation of helical flows even further. Such behavior has not been observed in tidal channels flanked by vegetated intertidal plain, wherein V_P and V_S maxima are approximately in phase and correspond roughly to near-bankfull water stages (e.g., Fagherazzi et al., 2008; Finotello, Ghinassi, et al., 2020; Kearney et al., 2017). Additionally, secondary circulations also appear poorly developed at the confluence site. It is well known that complex circulation patterns can arise at channel confluences (e.g., Lane et al., 2000; Leite Ribeiro et al., 2012; Rhoads & Kenworthy, 1995; Schindfessel et al., 2015), which are likely to suppress curvature-induced secondary flows. Nonetheless, one should appreciate that channel confluences in intertidal mudflat channel networks are somehow less frequent than in networks carving vegetated intertidal plains, owing to the lower drainage density that characterizes bare intertidal areas (e.g., Kearney & Fagherazzi, 2016). Therefore, flow disturbances and helical flow disruption due to channel confluences and bifurcations are not likely to have a significant limiting effect on meander morphodynamics in intertidal mudflats.

Overall, the results we illustrated so far suggest poor development of curvature-induced secondary flows in intertidal mudflat meander bends. The implications

of this hydrodynamic peculiarity, as well as those highlighted in Section 5.1, for the morphodynamics of intertidal mudflat meanders, will be discussed in the next section.

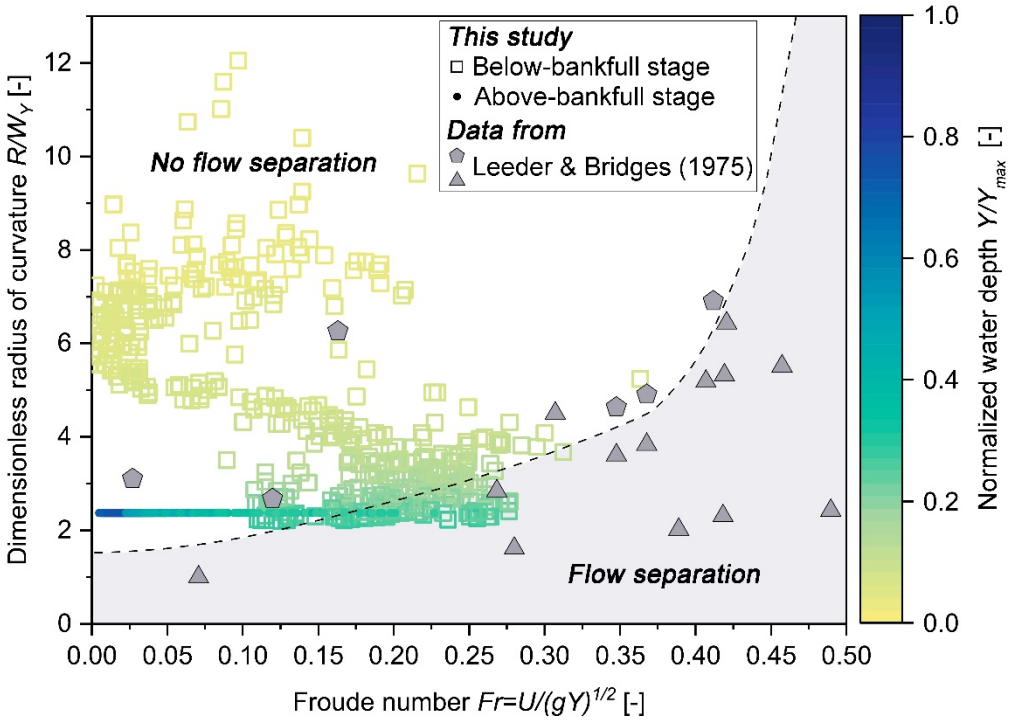

Figure 12. Flow separation in tidal meander bends according to Leeder & Bridges (1975). The normalized radius of curvature ($\frac{R}{W_Y}$) is plotted as a function of Froude number (Fr) for distinct tidal flow depth (Y) and velocity (U) at the apex of the studied meander bend. The parameter W_Y represents the effective bend width corresponding to different water depths (Y), whereas Fr is calculated for different water depths Y and the corresponding uniform flow velocities U, the latter being approximated by the depth-averaged velocity (DAV). Colors denote varying normalized water depths, computed as the ratio between instantaneous water depths and the maximum water depth ($Y_{\max}$) observed during the entire monitoring timespan. Filled dots denote below-bankfull water stages ($Y<Y_b$, where Y_b is the bankfull depth), whereas empty squares highlight above-bankfull stages ($Y>Y_b$). Original data points from Leeder and Bridges (1975) are also reported using gray markers, along with their empirical line separating bends with and without flow separation.

5.3 Implications for meander morphodynamics

Since the generation and propagation of helical flow are hampered, questions arise regarding what are the chief morphodynamic processes driving meander evolution in unvegetated intertidal mudflats. Previous studies suggested that

mudflat meanders can form and develop without significant secondary circulations. For example, the evolution of small mudflat meandering channels (about 1 m wide) in the Westerschelde estuary (Netherlands) was found to be primarily driven by late-ebb flows, which determined the erosion of channel bed due to backward-migrating steps generated by hydraulic jumps, which in turn promoted channel bank erosion due to bank undercutting and pronounced flow separation in sharp bends (Kleinhans et al., 2009). In our studied channel, sustained velocities at low water stages (Figures 5,6,8,9,10,11), together with direct visual inspections of sustained flow velocities near the end of ebb tides (see Figure 4), support the idea proposed by Kleinhans et al. (2009) that the morphodynamics of intertidal mudflat meanders is strongly controlled by late-ebb flows rather than by classic bar-hugging helical flow produced by curvature-induced secondary flows at high-water stages. Reduced control of helical flows on channel morphodynamics is also testified by the symmetric, V-shaped form of the studied channel cross-sections (Figure 4b), which attests to the scarce development of secondary (i.e., cross-sectional) flows and contrasts with the asymmetrical U-shaped cross-sections displayed by meandering channels in vegetated tidal marshes (Finotello, Ghinassi, et al., 2020; Zhao et al., 2022).

In contrast to late-ebb flows, we speculate that tidal flows at early-flood stages are not likely to have significant effects in terms of bank undercutting and sediment transport because velocities increase more slowly than during late ebb, and rates of water depth change through time ($\dot{Y}$), though sustained, do not produce significant variations in DAVs (Figure 6). Our analyses indeed confirm that tidal flows tend to be ebb-dominated at low water depths (Figure 5e,f), and also highlight that at $Y<Y_B$ ebb velocities attain values close to the maximum for much longer periods than during the flood (Figure 6), thus likely enhancing the morphodynamic control of late-ebb flows on channel evolution. Moreover, late-ebb flows are likely to occur even for tidal oscillations lower than those we monitored here, whereas pronounced overbank flows and related secondary circulations require significant tidal oscillations to be formed. Because intense late-ebb flows act at every tidal cycle and operate for extended periods, the total morphodynamic work they produce is in all likelihood much more significant than that produced during other tidal phases, further supporting the hypothesis that late-ebb tidal stages are the most morphodynamically relevant for mudflat meander evolution.

The above-described morphodynamic control of late-ebb stages is likely to be even more relevant compared to vegetated tidal landscapes due to the absence of vegetation not only on intertidal plains but also within tidal channels. In fact, previous studies focusing on salt-marsh channels demonstrated how in-channel aquatic vegetation can enhance bottom roughness and flow turbulence (e.g., Finotello, Ghinassi, et al., 2020; Folkard, 2005), further limiting tidal flow velocities at low stages, especially in relatively small channels with widths comparable to the characteristic size of vegetation patches. The presence of aquatic vegetation would clearly prevent significant morphodynamic work to be performed by late-ebb tidal stages, which is likely not the case in the unvegetated

mudflat channel we investigated here.

In addition to the above, meander morphodynamics in unvegetated intertidal flats can also be driven by episodic and seasonal increases in discharges due to heavy rainfalls and melting snows (Choi et al., 2013; Choi & Jo, 2015). Choi (2011, 2014) observed that these episodic events are likely to cause abrupt morphologic changes, pronounced point bar migration, frequent meander-bend cut-off, as well as channel abandonments. Particularly, significant rainfall-induced runoff during low tides would mimick late-ebb flows, thus further increasing the morphodynamic relevance of seaward-directed, shallow, in-channel flows. New field measurements will however be required to support this hypothesis in the Yangkou tidal flat, since the data presented in this study were collected in October, which is outside the monsoon season.

Storm waves could also induce bank collapses in unvegetated tidal channels (Choi, 2011; Choi & Jo, 2015; Ghinassi et al., 2019), thus critically affecting meander morpho-sedimentary evolution. In spite of the absence of vegetation that can help stabilize banks and prevent erosion, no collapsed slump blocks were observed within our study channel (Gabet, 1998; Hackney et al., 2015), although such blocks could be easily disgregated and removed, once formed, by sustained in-channel velocities combined with the absence of additional cohesion given by vegetation roots.

Bank collapses can also form due to significant tidal oscillations and pore-excess pressure between channel and banks driven by rapid changes in water levels (Zhao et al., 2022; Zhao et al., 2019), which generate significant seepage flows (e.g., Gardner & Wilson, 2006; Wilson & Morris, 2012). Seepage flows during late-ebb tides, also favored by extensive bioturbation due to fiddler-crab and mudskipper burrowing (Harvey et al., 2019; Ishimatsu et al., 1998; Perillo et al., 2005; Xin et al., 2022), are likely responsible for the widespread bank slumps that we observed at the middle and lower portions of channel cross-sections in the studied channel (Figure 13). Notably, strong seepage flows can also help explain why sustained velocities are observed over nearly the entire duration of the ebb phase (Figure 6 a,b,c,d), and further support the idea that the ebb-late phases exert a strong control on the morphodynamics of intertidal mudflat meanders.

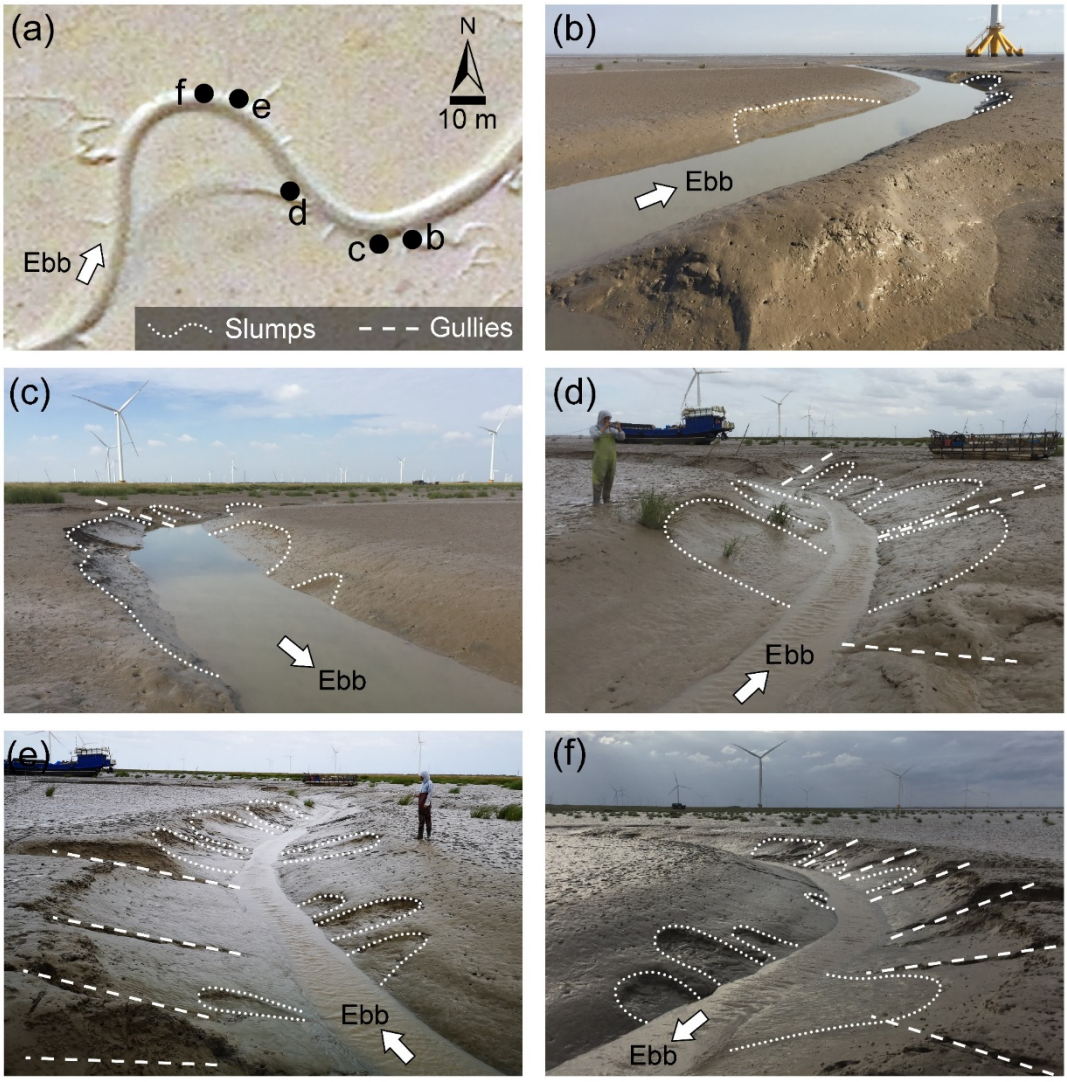

Figure 13. Bank erosion along the studied channel. (a) Locations of the photographs. (b,c,d,e,f) Close-up views of bank slumps (white dotted lines) and gullies (white dashed lines) along the studied channel. All photos were taken during ebb tides.

If, on the one hand, bank collapses driven by seepage flow are also commonly documented in vegetated macrotidal settings (Cosma et al., 2022; Zhao et al., 2022) and are therefore more closely linked to sustained tidal oscillations, on the other hand, the abundant erosional gullies (Figure 13) observed at channel banks are most likely specific of unvegetated settings. The formation of such gullies, which can significantly contribute to bank erosion processes, is promoted

by strong erosion at the ebb-bankfull transition and favored by the absence of vegetation cover (Guimond & Tamborski, 2021). Bank collapses and gullies can also be counterintuitively related to the presence of cohesive extracellular polymeric substances (EPS) generated by microorganisms abundant on intertidal flats. However, although EPS are widely regarded as bed "stabilizers" (Flemming & Wuertz, 2019), recent flume experiments show that they may enhance sediment mobility under wave actions, inducing liquefaction of otherwise stable bank sediment (Chen et al., 2021), with clear implications for the dynamics of meandering tidal channels.

Overall, our results support the idea that meander evolution in intertidal mudflats might not be necessarily correlated with classic curvature-induced helical flows at near-bankfull stages, and that other ecomorphodynamic factors, most likely related to tidal hydrodynamics at late-ebb stages, can be more relevant for meander morphodynamics. A conceptual summary sketch illustrating the major hydrodynamic and morphodynamic differences between tidal meandering channels in vegetated and unvegetated contexts is shown in Figure 14. Further analyses will be needed to corroborate the inferences presented in this study, as well as to investigate the role played by different tidal amplitudes on the processes we described here, especially in terms of distinct hydrodynamic behavior between above and below-bankfull stages. Nonetheless, large tidal ranges (relative to characteristic wind-wave heights) are needed for the development of intertidal mudflats (e.g., Friedrichs, 2011; Klein, 1985; Morales, 2022), so we argue that the processes observed in the present study are likely to be common also in intertidal mudflat channels different from the study case we analyzed here.

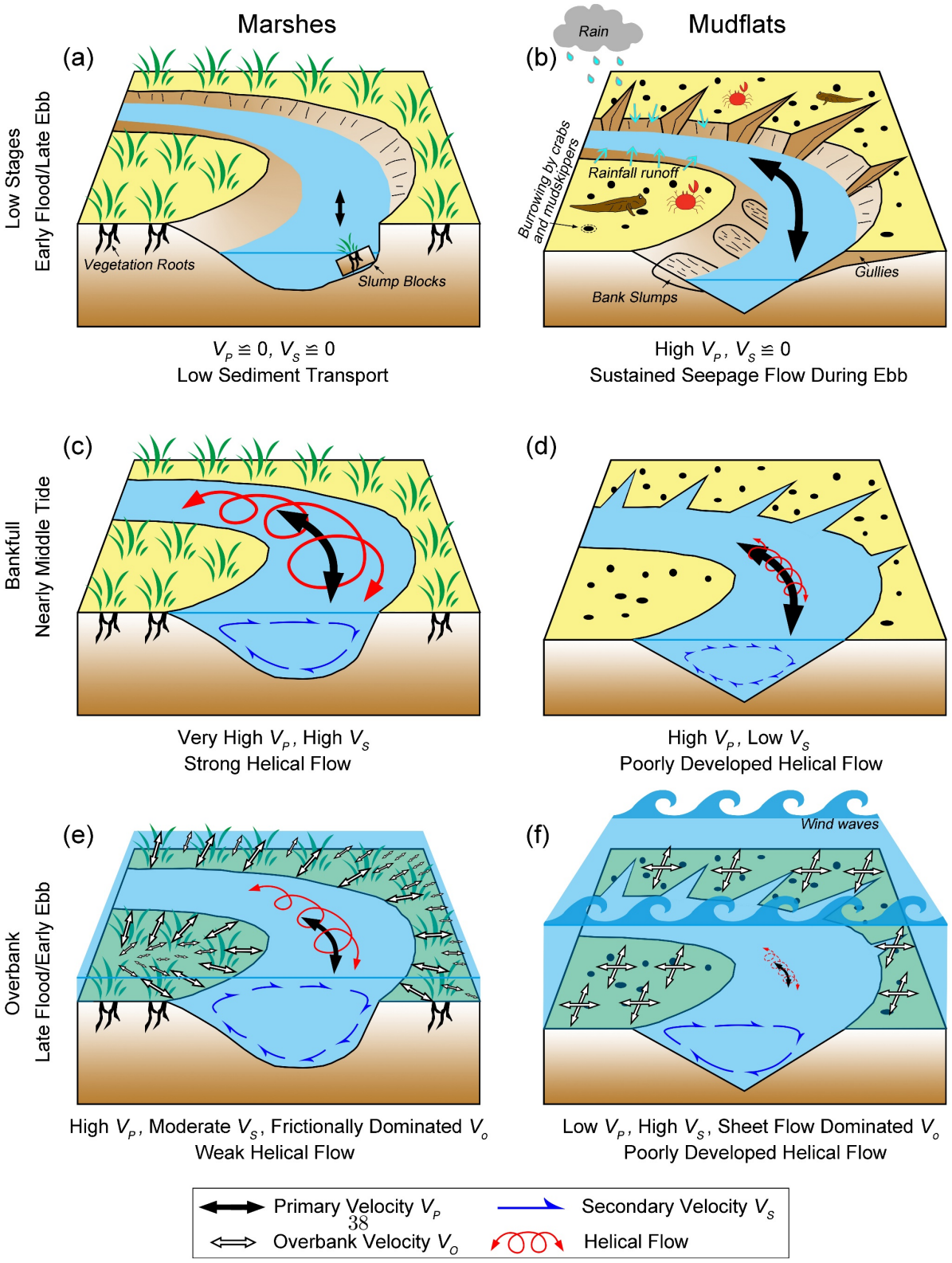
Marshes
Mudflats
(a)
(b)
Rain
Low Stages
Early Flood/Late Ebb
Vegetation Roots
Slump Blocks
Burrowing by crabs and mudskippers
Rainfall runoff
Gullies
Bank Slumps
$V_P \cong 0$, $V_S \cong 0$
Low Sediment Transport
High V_P, $V_S \cong 0$
Sustained Seepage Flow During Ebb
(c)
(d)
Bankfull
Nearly Middle Tide
Very High V_P, High V_S
Strong Helical Flow
High V_P, Low V_S
Poorly Developed Helical Flow
(e)
(f)
Overbank
Late Flood/Early Ebb
Wind waves
High V_P, Moderate V_S, Frictionally Dominated V_o
Weak Helical Flow
Low V_P, High V_S, Sheet Flow Dominated V_o
Poorly Developed Helical Flow
Primary Velocity V_P
Secondary Velocity V_S
Overbank Velocity V_O
Helical Flow

Figure 14. Conceptual sketch depicting the major differences of hydrodynamic processes observed in tidal channels dissecting vegetated (i.e., salt marshes, left columns) and unvegetated (i.e., mudflats, right columns) intertidal plains. (a, b) Channel hydrodynamics during below-bankfull water stages, with particular reference to early-flood and late-ebb stages; (c, d) Channel hydrodynamics at the bankfull stage; (e, f) Channel hydrodynamics during overbank stages.

6 Conclusions

This study contributes to the understanding of hydrodynamic flow structures, and related morphodynamic evolution, in meandering channels wandering through unvegetated tidal flats. Hydroacoustic measurements were carried out, for several tidal cycles, at distinct locations along a mudflat meander bend found within the macrotidal Yangkou tidal flat (Jiangsu province, China).

The main conclusions of this research can be summarized as follows:

1. Stage-velocity relationships in mudflat channels are different from those observed in channels wandering through vegetated intertidal plains (i.e., salt marsh and mangrove forests). Specifically, while in the latter case both ebb and flood velocities tend to be higher for above-bankfull water stages, in our study case we observed significantly larger velocities when tidal flows remained confined within the channel banks. This is likely because, in vegetated intertidal plains, both frictionally-dominated flow propagation and higher elevation of channel banks (relative to tidal excursions) ensure flow confinement and high in-channel velocities even for above-bankfull stages. In contrast, in unvegetated intertidal mudflats, similar flow resistance within and outside channels and lower elevation of channel banks produce widespread sheet flow at above-bankfull stages and limit in-channel velocities due to reduced flow confinement;

2. Secondary currents appear to be mostly related to flood flows, and are generally stronger during overbank stages. In some cases, however, the orientation of secondary circulations is reversed compared to classic flow models in meander bends. Poorly-developed secondary circulations are observed at the bend apex. However, primary flow separation, coupled with localized flow measurements that did not include the entire channel cross-section, have likely limited our ability to detect secondary circulation cells during our field measurements.

3. Field data collectively suggest limited control of curvature-induced helical flows on meander morphodynamics. This is most likely due to a consistent phase lag between maxima of primary (i.e., streamwise) and secondary (i.e., cross-sectional) velocities. Such a lag effectively limits the landward (seaward) transfer of secondary flows during the flood (ebb) phase, thus hampering the formation of coherent helical flow structures along the entire meander bends. These findings support the results of earlier studies that suggested that, in stark contrast with both river and salt-marsh meandering channels, meander morphodynamics in intertidal

mudflats are poorly related to bankfull hydrodynamics, in general, and curvature-induced helical flows in particular.

4. We suggest that other morphodynamic processes drive the evolution of intertidal mudflat meander bends. Late-ebb tidal flows likely exert strong control on meander morphodynamics due to sustained velocities and pronounced seepage flows, which determine significant sediment transport as well as both bank undercutting and collapses. These effects are also possibly amplified by the absence of vegetation both within and outside the channel, as well as by significant bioturbation of the channel banks, which reduces bank resistance to erosion and enhances seepage flow. In addition, storm waves and both episodic and seasonal increases in discharges due to heavy rainfalls (e.g., related to the monsoon season) and melting snows can compound the morphological effects of late-ebb flows, producing abrupt morphologic changes and pronounced channel migration.

Additional field and modeling efforts would be required to corroborate the inferences presented in this study and to investigate how different tidal ranges and channel-bank elevations (relative to characteristic tidal oscillations) affect mudflat meander hydrodynamics and the related morphodynamic evolution. Particularly, cross-sectional measurements of tidal flow fields are needed to directly assess the scarce development of curvature-induced helical flows, whereas repeated measurement of flow fields during normal conditions and heavy rainfall events, coupled with morphological monitoring of channel bank evolution, would help clarify the relative importance of astronomic and meteorological forcings on the morphodynamics of intertidal mudflat meanders.

Acknowledgments

This study was financially supported by the National Natural Science Foundation of China (U2240220, 41625021), the Innovation Program of Shanghai Municipal Education Commission (2019-01-07-00-05-E00027), the China Scholarship Council (CSC) scholarships (202106190084) and Jiangsu Special Program for Science and Technology Innovation (JSZRHYKJ2021006). We thank Zhenqiao Liu, Wei Feng, Jianxiong Sun, and Dongyun Wei for their help in field work. Special acknowledgments are given to Shibing Zhu for his help in grain size analysis.

Open Research

The data sets generated and/or analyzed during the current study are freely available at https://doi.org/10.6084/m9.figshare.20161733.v2

References

https://doi.org/10.1002/2017GL075721

https://doi.org/10.1038/269504a0

https://doi.org/10.1016/0302-3524(79)90038-0

https://doi.org/10.1002/hyp.10690
https://doi.org/10.1029/2008JF001137
https://doi.org/10.1029/2010JF001806
https://doi.org/10.1029/2003WR002068
https://doi.org/10.1002/esp.3324
https://doi.org/10.4319/lo.1975.20.1.0071
https://doi.org/10.1007/s10750-004-7149-0
https://doi.org/10.1111/j.1365-3091.1982.tb01732.x
https://doi.org/10.1016/j.sedgeo.2016.08.005
https://doi.org/10.1002/esp.4912
https://doi.org/10.1029/2001JC001082
https://doi.org/10.1029/2020GL092137
https://doi.org/10.2110/jsr.2010.054
https://doi.org/10.1016/j.margeo.2011.05.002
https://doi.org/10.1016/j.ocecoaman.2014.07.009
https://doi.org/10.1016/j.margeo.2013.10.005
https://doi.org/10.2110/jsr.2015.44
https://doi.org/10.1006/ecss.2000.0548
https://doi.org/10.1016/j.margeo.2013.08.005
https://doi.org/10.1016/j.geomorph.2020.107402
https://doi.org/10.1111/sed.12942
https://doi.org/10.1016/j.geomorph.2007.04.013
https://doi.org/10.1029/2004JF000182
https://doi.org/10.1017/9781316888933.005
https://doi.org/10.1029/WR019i005p01173
https://doi.org/10.1029/2005WR004050
https://doi.org/10.1061/JYCEAJ.0004109
https://doi.org/10.1029/2007WR006289
https://doi.org/10.1029/2003WR001965
https://doi.org/10.1029/2019JF005193
https://doi.org/10.1002/esp.5396

https://doi.org/10.1038/s41598-019-56992-w
https://doi.org/10.1130/G46761C.1
https://doi.org/10.1029/2020WR027822
https://doi.org/10.1038/s41579-019-0158-9
https://doi.org/10.4319/lo.2005.50.5.1592
https://doi.org/10.1306/74D70C36-2B21-11D7-8648000102C1865D
https://doi.org/10.1016/0272-7714(88)90082-0
https://www.jstor.org/stable/25736162
https://doi.org/10.1002/esp.471
https://doi.org/10.2307/1353278
https://doi.org/10.1016/j.ecss.2006.05.009
https://doi.org/10.1029/2021WR030840
https://doi.org/10.1111/sed.12616
https://doi.org/10.1061/(Asce)0733-9429(2002)128:1(117
https://doi.org/10.1175/JTECH-D-16-0148.1
https://doi.org/10.3390/w13040543
https://doi.org/10.1029/2018JC014372
https://doi.org/10.1002/2015GL066481
https://agupubs.onlinelibrary.wiley.com/doi/abs/10.1029/2018RG000635
https://doi.org/10.1007/978-1-4020-3609-5_134
https://doi.org/10.1130/0016-7606(1975)86
https://doi.org/10.1016/B978-0-12-374739-6.00241-4
https://doi.org/10.1002/esp.5124
https://doi.org/10.1007/978-94-007-0123-6_11
https://doi.org/10.1038/34560
https://doi.org/10.1038/ncomms12287
https://doi.org/10.1002/lom3.10168
https://doi.org/10.1016/B978-0-444-63529-7.00006-7
https://doi.org/10.1061/(ASCE)0733-9429(2000)126:6(399
https://doi.org/10.1038/nature12856
https://doi.org/10.1007/978-1-4612-5078-4_3

https://doi.org/10.1016/j.geomorph.2008.10.005
https://doi.org/10.1175/JPO-D-18-0175.1
https://doi.org/10.1002/1099-1085(20000815/30)14:11/12
https://doi.org/10.1038/253338a0
https://doi.org/10.1029/2011JF002171
https://doi.org/10.1306/212F8FB7-2B24-11D7-8648000102C1865D
https://doi.org/10.1016/j.ecss.2019.106524
https://doi.org/10.1007/978-3-030-96121-3_20
https://doi.org/10.1038/s41586-018-0805-8
https://doi.org/10.1126/science.abm9583
https://doi.org/10.1175/2008JPO4017.1
https://doi.org/10.1002/esp.3367
https://doi.org/10.1007/978-3-319-99194-8_10
https://doi.org/10.1002/2016JC012623
https://doi.org/10.1007/s00367-005-0209-2
https://doi.org/10.1126/science.1093515
https://doi.org/10.1007/BF01507352
https://doi.org/10.1016/0278-4343(86)90037-3
https://doi.org/10.1016/0169-555X(94)00069-4
https://doi.org/10.1029/1999WR900237
https://doi.org/10.1029/1999WR900238
https://doi.org/10.1002/9781119117261.ch10
https://doi.org/10.3390/w7094724
https://doi.org/10.1038/s41467-022-29654-1
https://doi.org/10.1029/2020WR028577
https://doi.org/10.1016/j.jher.2016.01.002
https://doi.org/10.1016/j.ecss.2016.11.008
https://doi.org/10.2110/jsr.2012.21
https://doi.org/10.1017/S0022112001006565
https://doi.org/10.1016/j.scitotenv.2020.139503
https://doi.org/10.1016/j.ecss.2021.107687

https://doi.org/10.1002/2014JF003365

https://doi.org/10.1038/nature12859

https://doi.org/10.1002/esp.2095

https://doi.org/10.1038/315746a0

https://doi.org/10.1029/2018JC014281

https://doi.org/10.1098/rspa.2015.0115

https://doi.org/10.1016/j.geomorph.2014.11.020

https://doi.org/10.1016/j.csr.2004.05.006

https://doi.org/10.1038/s41558-020-0697-0

https://doi.org/10.1016/S0037-0738(97)00026-2

https://doi.org/10.1002/jgrc.20340

https://doi.org/10.1016/0025-3227(90)90044-K

http://doi.org/10.1007/s10533-010-9570-y

https://doi.org/10.1016/j.margeo.2011.06.006

https://doi.org/10.2112/JCOASTRES-D-18-00006.1

https://doi.org/10.1016/j.earscirev.2014.07.006

https://doi.org/10.1029/2019WR025514

https://doi.org/10.3390/ijerph17093191

Azpiroz-Zabala, M., Cartigny, M. J. B., Sumner, E. J., Clare, M. A., Talling, P. J., Parsons, D. R., & Cooper, C. (2017). A General Model for the Helical Structure of Geophysical Flows in Channel Bends. *Geophysical Research Letters, 44*(23), 11,932-911,941. Bathurst, J. C., Thorne, C. R., & Hey, R. D. (1977). Direct measurements of secondary currents in river bends. *Nature, 269*(5628), 504-506. Bayliss-Smith, T. P., Healey, R., Lailey, R., Spencer, T., & Stoddart, D. R. (1979). Tidal flows in salt marsh creeks. *Estuarine and Coastal Marine Science, 9*(3), 235-255. Bever, A. J., & MacWilliams, M. L. (2016). Factors influencing the calculation of periodic secondary circulation in a tidal river: numerical modelling of the lower Sacramento River, USA. *Hydrological processes, 30*(7), 995-1016. Blanckaert, K. (2009). Saturation of curvature-induced secondary flow, energy losses, and turbulence in sharp open-channel bends: Laboratory experiments, analysis, and modeling. *Journal of Geophysical Research: Earth Surface, 114*(F3). Blanckaert, K. (2011). Hydrodynamic processes in sharp meander bends and their morphological implications. *Journal of Geophysical Research: Earth Surface, 116*(F1). Blanckaert, K., & de Vriend, H. J. (2003). Nonlinear modeling of mean flow redistribution in curved open channels. *Water Resources Research, 39*(12). Blanckaert, K., Kleinhans, M. G., McLelland, S. J., Uijttewaal, W. S. J., Murphy, B. J., van de Kruijs, A., et al. (2013). Flow

separation at the inner (convex) and outer (concave) banks of constant-width and widening open-channel bends. *Earth Surface Processes and Landforms, 38*(7), 696-716. Boon, J. D. (1975). Tidal discharge asymmetry in a salt marsh drainage system1,2. *Limnology and Oceanography, 20*(1), 71-80. Bouma, T. J., Vries, M. B. D., Low, E., Kusters, L., Herman, P. M. J., Tánczos, I. C., et al. (2005). Flow hydrodynamics on a mudflat and in salt marsh vegetation: identifying general relationships for habitat characterisations. *Hydrobiologia, 540*(1-3), 259-274. Bridge, J. S., & Jarvis, J. (1982). The dynamics of a river bend: a study in flow and sedimentary processes. *Sedimentology, 29*(4), 499-541. Brivio, L., Ghinassi, M., D'Alpaos, A., Finotello, A., Fontana, A., Roner, M., & Howes, N. (2016). Aggradation and lateral migration shaping geometry of a tidal point bar: An example from salt marshes of the Northern Venice Lagoon (Italy). *Sedimentary Geology, 343*, 141-155. Brooks, H., Möller, I., Carr, S., Chirol, C., Christie, E., Evans, B., et al. (2021). Resistance of salt marsh substrates to near-instantaneous hydrodynamic forcing. *Earth Surface Processes and Landforms, 46*(1), 67-88. Chant, R. J. (2002). Secondary circulation in a region of flow curvature: Relationship with tidal forcing and river discharge. *Journal of Geophysical Research, 107*(C9). Chen, J. D. (2016). *Sediment dynamic process on tidal flat under windy conditions.* (Master), Nanjing University, Nanjing. Chen, X., Zhang, C., H. Townend, I., Paterson, D. M., Gong, Z., Jiang, Q., et al. (2021). Biological Cohesion as the Architect of Bed Movement Under Wave Action. *Geophysical Research Letters, 48*(5), e2020GL092137. Choi, K. (2010). Rhythmic Climbing-Ripple Cross-Lamination in Inclined Heterolithic Stratification (IHS) of a Macrotidal Estuarine Channel, Gomso Bay, West Coast of Korea. *Journal of Sedimentary Research, 80*(6), 550-561. Choi, K. (2011). External controls on the architecture of inclined heterolithic stratification (IHS) of macrotidal Sukmo Channel: Wave versus rainfall. *Marine Geology, 285*(1-4), 17-28. Choi, K. (2014). Morphology, sedimentology and stratigraphy of Korean tidal flats – Implications for future coastal managements. *Ocean & Coastal Management, 102*, 437-448. Choi, K., Hong, C. M., Kim, M. H., Oh, C. R., & Jung, J. H. (2013). Morphologic evolution of macrotidal estuarine channels in Gomso Bay, west coast of Korea: Implications for the architectural development of inclined heterolithic stratification. *Marine Geology, 346*, 343-354. Choi, K., & Jo, J. (2015). Morphodynamics of tidal channels In the Open Coast Macrotidal Flat, Southern Ganghwa Island In Gyeonggi Bay, West Coast of Korea. *Journal of Sedimentary Research, 85*(6), 582-595. Christiansen, T., Wiberg, P. L., & Milligan, T. G. (2000). Flow and Sediment Transport on a Tidal Salt Marsh Surface. *Estuarine, Coastal and Shelf Science, 50*(3), 315-331. Coco, G., Zhou, Z., van Maanen, B., Olabarrieta, M., Tinoco, R., & Townend, I. (2013). Morphodynamics of tidal networks: Advances and challenges. *Marine Geology, 346*, 1-16. Cosma, M., Finotello, A., Ielpi, A., Ventra, D., Oms, O., D'Alpaos, A., & Ghinassi, M. (2020). Piracy-controlled geometry of tide-dominated point bars: Combined evidence from ancient sedimentary successions and modern channel networks. *Geomorphology, 370*. Cosma, M., Lague, D., D'Alpaos, A., Leroux, J., Feldmann, B., & Ghinassi, M. (2022). Sedimentology of a hypertidal point bar (Mont-Saint-Michel Bay, north-western France)

revealed by combining lidar time-series and sedimentary core data. *Sedimentology, 69*(3), 1179-1208. D'Alpaos, A., Lanzoni, S., Marani, M., Bonometto, A., Cecconi, G., & Rinaldo, A. (2007). Spontaneous tidal network formation within a constructed salt marsh: Observations and morphodynamic modelling. *Geomorphology, 91*(3-4), 186-197. D'Alpaos, A., Lanzoni, S., Marani, M., Fagherazzi, S., & Rinaldo, A. (2005). Tidal network ontogeny: Channel initiation and early development. *Journal of Geophysical Research-Earth Surface, 110*(F2). D'Alpaos, A., Finotello, A., Goodwin, G. C. H., & Mudd, S. M. (2021). Salt Marsh Hydrodynamics. In *Salt Marshes* (pp. 53-81). Dietrich, W. E. (1987). Mechanics of flow and sediment transport in river bends. In K. S. Richards (Ed.), *River Channels: Environment and Process* (Vol. 18, pp. 179-227). Institute of British Geographers, Special Publication: Blackwell Oxford.Dietrich, W. E., & Smith, J. D. (1983). Influence of the point bar on flow through curved channels. *Water Resources Research, 19*(5), 1173-1192. Dinehart, R. L., & Burau, J. R. (2005). Averaged indicators of secondary flow in repeated acoustic Doppler current profiler crossings of bends. *Water Resources Research, 41*(9). Engelund, F. (1974). Flow and Bed Topography in Channel Bends. *Journal of the Hydraulics Division, 100*(11), 1631-1648. Fagherazzi, S., Hannion, M., & D'Odorico, P. (2008). Geomorphic structure of tidal hydrodynamics in salt marsh creeks. *Water Resources Research, 44*(2). Ferguson, R. I., Parsons, D. R., Lane, S. N., & Hardy, R. J. (2003). Flow in meander bends with recirculation at the inner bank. *Water Resources Research, 39*(11). Finotello, A., Canestrelli, A., Carniello, L., Ghinassi, M., & D'Alpaos, A. (2019). Tidal flow asymmetry and discharge of lateral tributaries drive the evolution of a microtidal meander in the Venice Lagoon (Italy). *Journal of Geophysical Research: Earth Surface, 124*(12), 3043-3066. Finotello, A., Capperucci, R. M., Bartholomä, A., D'Alpaos, A., & Ghinassi, M. (2022). Morpho-sedimentary evolution of a microtidal meandering channel driven by 130-years of natural and anthropogenic modifications of the Venice Lagoon (Italy). *Earth Surface Processes and Landforms, n/a*(n/a), 1-17. Finotello, A., D'Alpaos, A., Bogoni, M., Ghinassi, M., & Lanzoni, S. (2020). Remotely-sensed planform morphologies reveal fluvial and tidal nature of meandering channels. *Scientific Reports, 10*(1), 54. Finotello, A., D'Alpaos, A., Lazarus, E. D., & Lanzoni, S. (2019). High curvatures drive river meandering: COMMENT. *Geology, 47*(10), e485. Finotello, A., Ghinassi, M., Carniello, L., Belluco, E., Pivato, M., Tommasini, L., & D'Alpaos, A. (2020). Three-Dimensional flow structures and morphodynamic evolution of microtidal meandering channels. *Water Resources Research, 56*(7). Flemming, H.-C., & Wuertz, S. (2019). Bacteria and archaea on Earth and their abundance in biofilms. *Nature Reviews Microbiology, 17*(4), 247-260. Folkard, A. M. (2005). Hydrodynamics of model Posidonia oceanica patches in shallow water. *Limnology and Oceanography, 50*(5), 1592-1600. Friedman, G. M. (1962). Comparison of moment measures for sieving and thin-section data in sedimentary petrological studies. *Journal of Sedimentary Research, 32*(1), 15-25. Friedrichs, C. T. (2011). Tidal Flat Morphodynamics: A Synthesis. In J. D. Hansom & B. W. Fleming (Eds.), *Treatise on Estuarine and Coastal Science* (Vol. 3, pp. 137-170). Amsterdam, Netherlands: Elsevier. https://doi.org/10.1016/B978-0-12-374711-

2.00307-7Friedrichs, C. T., & Aubrey, D. G. (1988). Non-linear tidal distortion in shallow well-mixed estuaries: a synthesis. *Estuarine, Coastal and Shelf Science, 27*(5), 521-545. Friedrichs, C. T., & Perry, J. E. (2001). Tidal salt marsh morphodynamics: a synthesis. *Journal of Coastal Research*, 7-37. Frothingham, K. M., & Rhoads, B. L. (2003). Three-dimensional flow structure and channel change in an asymmetrical compound meander loop, Embarras River, Illinois. *Earth Surface Processes and Landforms, 28*(6), 625-644. Gabet, E. J. (1998). Lateral Migration and Bank Erosion in a Saltmarsh Tidal Channel in San Francisco Bay, California. *Estuaries, 21*(4). Gao, S. (2019). Geomorphology and Sedimentology of Tidal Flats. In *Coastal Wetlands* (pp. 359-381): Elsevier. https://doi.org/10.1016/B978-0-444-63893-9.00010-1Gardner, L. R., & Wilson, A. M. (2006). Comparison of four numerical models for simulating seepage from salt marsh sediments. *Estuarine, Coastal and Shelf Science, 69*(3), 427-437. Geng, L., D'Alpaos, A., Sgarabotto, A., Gong, Z., & Lanzoni, S. (2021). Intertwined Eco-Morphodynamic Evolution of Salt Marshes and Emerging Tidal Channel Networks. *Water Resources Research, 57*(11), e2021WR030840. Ghinassi, M., D'Alpaos, A., Tommasini, L., Brivio, L., Finotello, A., Stefani, C., & Walsh, J. P. (2019). Tidal currents and wind waves controlling sediment distribution in a subtidal point bar of the Venice Lagoon (Italy). *Sedimentology, 66*(7), 2926-2949. Goring, D. G., & Nikora, V. I. (2002). Despiking acoustic Doppler velocimeter data. *Journal of Hydraulic Engineering-Asce, 128*(1), 117-126.)Guerra, M., & Thomson, J. (2017). Turbulence Measurements from Five-Beam Acoustic Doppler Current Profilers. *Journal of Atmospheric and Oceanic Technology, 34*(6), 1267-1284. Guimond, J., & Tamborski, J. (2021). Salt Marsh Hydrogeology: A Review. *Water, 13*(4), 543. Guo, L., Wang, Z. B., Townend, I., & He, Q. (2019). Quantification of Tidal Asymmetry and Its Nonstationary Variations. *Journal of Geophysical Research: Oceans, 124*(1), 773-787. Hackney, C., Best, J., Leyland, J., Darby, S. E., Parsons, D., Aalto, R., & Nicholas, A. (2015). Modulation of outer bank erosion by slump blocks: Disentangling the protective and destructive role of failed material on the three-dimensional flow structure. *Geophysical Research Letters, 42*(24), 10,663-610,670. Harvey, G. L., Henshaw, A. J., Brasington, J., & England, J. (2019). Burrowing Invasive Species: An Unquantified Erosion Risk at the Aquatic-Terrestrial Interface. *Reviews of Geophysics, 57*(3), 1018-1036. Hickin, E. J. (1978). Meandering channels. In G. V. Middleton, M. J. Church, M. Coniglio, L. A. Hardie, & F. J. Longstaffe (Eds.), *Encyclopedia of Sediments and Sedimentary Rocks* (pp. 703-709). Dordrecht: Springer Netherlands. Hickin, E. J., & Nanson, G. C. (1975). The Character of Channel Migration on the Beatton River, Northeast British Columbia, Canada. *Geological Society of America Bulletin, 86*(4), 487-494. <487:TCOCMO>2.0.CO;2Hooke, J. M. (2013). River Meandering. In J. Shroder & E. Wohl (Eds.), *Treatise on Geomorphology* (Vol. 9, pp. 260-288). San Diego, CA: Academic Press. Horstman, E. M., Bryan, K. R., & Mullarney, J. C. (2021). Drag variations, tidal asymmetry and tidal range changes in a mangrove creek system. *Earth Surface Processes and Landforms, 46*(9), 1828-1846. Hughes, Z. J. (2012). Tidal Channels on Tidal Flats and Marshes. In R. A. Davis Jr & R. W. Dalrymple (Eds.), *Principles of Tidal Sedimentology*

(pp. 269-300). Dordrecht: Springer Netherlands. Ishimatsu, A., Hishida, Y., Takita, T., Kanda, T., Oikawa, S., Takeda, T., & Huat, K. K. (1998). Mudskippers store air in their burrows. *Nature, 391*(6664), 237-238. Kearney, W. S., & Fagherazzi, S. (2016). Salt marsh vegetation promotes efficient tidal channel networks. *Nature Communications, 7*(1), 12287. Kearney, W. S., Mariotti, G., Deegan, L. A., & Fagherazzi, S. (2017). Stage-discharge relationship in tidal channels. *Limnology and Oceanography: Methods, 15*(4), 394-407. Keevil, C. E., Parsons, D. R., Keevil, G. M., & Ainsley, M. (2015). Three-dimensional meander bend flow within the tidally influenced fluvial zone. In P. J. Ashworth, J. L. Best, & D. R. Parsons (Eds.), *Developments in Sedimentology* (Vol. 68, pp. 127-148): Elsevier. Kim, S. C., Friedrichs, C. T., Maa, J. P. Y., & Wright, L. D. (2000). Estimating bottom stress in tidal boundary layer from acoustic Doppler velocimeter data. *Journal of Hydraulic Engineering, 126*(6), 399-406.)Kirwan, M. L., & Megonigal, J. P. (2013). Tidal wetland stability in the face of human impacts and sea-level rise. *Nature, 504*(7478), 53-60. Klein, G. d. (1985). Intertidal flats and intertidal sand bodies. In R. A. Davis (Ed.), *Coastal sedimentary environments* (pp. 187-224). New York: Springer. Kleinhans, M. G., Schuurman, F., Bakx, W., & Markies, H. (2009). Meandering channel dynamics in highly cohesive sediment on an intertidal mud flat in the Westerschelde estuary, the Netherlands. *Geomorphology, 105*(3-4), 261-276. Kranenburg, W. M., Geyer, W. R., Garcia, A. M. P., & Ralston, D. K. (2019). Reversed Lateral Circulation in a Sharp Estuarine Bend with Weak Stratification. *Journal of Physical Oceanography, 49*(6), 1619-1637. Lan, T. F., Wu, H., Tang, J. P., Li, Z., & Wang, Y. P. (2019). A preliminary study on in situ bottom boundary layer measurement near the seabed of estuaries by using a novel high-frequency Acoustic Doppler Current Profiler (in Chinese). *Marine Science Bulletin, 38*(6), 640-649. Lane, S. N., Bradbrook, K. F., Richards, K. S., Biron, P. M., & Roy, A. G. (2000). Secondary circulation cells in river channel confluences: measurement artefacts or coherent flow structures? *Hydrological processes, 14*(11-12), 2047-2071. <2047::AID-HYP54>3.0.CO;2-4Leeder, M. R., & Bridges, P. H. (1975). Flow separation in meander bends. *Nature, 253*(5490), 338-339. Leite Ribeiro, M., Blanckaert, K., Roy, A. G., & Schleiss, A. J. (2012). Flow and sediment dynamics in channel confluences. *Journal of Geophysical Research: Earth Surface, 117*(F1). Li, H. Q., Yin, Y., Shi, Y., He, C. H., & Liu, X. Y. (2011). Micro-morphology and contemporary sedimentation rate of tidal flat in Rudong, Jiangsu Province (in Chinese). *Journal of Palaeogeography, 13*(02), 150-160. Liaghat, A., Mohammadi, K., & Rahmanshahi, M. (2014). 3D investigation of flow hydraulic in U shape meander bends with constant, decreasing and increasing width. *Journal of river engineering, 2*(3), 12-23. Liu, Z. X., Huang, Y. C., & Zhang, Q. N. (1989). Tidal current ridges in the Southwestern Yellow Sea. *Journal of Sedimentary Petrology, Vol. 59*, 432-437. McLachlan, R. L., Ogston, A. S., Asp, N. E., Fricke, A. T., Nittrouer, C. A., & Gomes, V. J. C. (2020). Impacts of tidal-channel connectivity on transport asymmetry and sediment exchange with mangrove forests. *Estuarine, Coastal and Shelf Science, 233*, 106524. Morales, J. A. (2022). Tide-Dominated Systems II: Tidal Flats and Wetlands. In J. A. Morales (Ed.), *Coastal Geology* (pp. 289-307).

Cham: Springer International Publishing. Murray, N. J., Phinn, S. R., DeWitt, M., Ferrari, R., Johnston, R., Lyons, M. B., et al. (2019). The global distribution and trajectory of tidal flats. *Nature, 565*(7738), 222-225. Murray, N. J., Worthington, T. A., Bunting, P., Duce, S., Hagger, V., Lovelock, C. E., et al. (2022). High-resolution mapping of losses and gains of Earth's tidal wetlands. *science, 376*(6594), 744-749. Nidzieko, N. J., Hench, J. L., & Monismith, S. G. (2009). Lateral Circulation in Well-Mixed and Stratified Estuarine Flows with Curvature. *Journal of Physical Oceanography, 39*(4), 831-851. Parsons, D. R., Ferguson, R. I., Lane, S. N., & Hardy, R. J. (2004). Flow structures in meander bends with recirculation zones: implications for bend movements. In C. Greco & D. Morte (Eds.), *River Flow* (pp. 49-57). London: Taylor & Francis.Parsons, D. R., Jackson, P. R., Czuba, J. A., Engel, F. L., Rhoads, B. L., Oberg, K. A., et al. (2013). Velocity Mapping Toolbox (VMT): a processing and visualization suite for moving-vessel ADCP measurements. *Earth Surface Processes and Landforms, 38*(11), 1244-1260. Passarelli, C., Hubas, C., & Paterson, D. M. (2018). Mudflat Ecosystem Engineers and Services. In P. G. Beninger (Ed.), *Mudflat Ecology* (pp. 243-269). Cham: Springer International Publishing. Pein, J., Valle-Levinson, A., & Stanev, E. V. (2018). Secondary Circulation Asymmetry in a Meandering, Partially Stratified Estuary. *Journal of Geophysical Research: Oceans, 123*(3), 1670-1683. Perillo, G. M. E., Minkoff, D. R., & Piccolo, M. C. (2005). Novel mechanism of stream formation in coastal wetlands by crab–fish–groundwater interaction. *Geo-Marine Letters, 25*(4), 214-220. Pilkey, O. H., & Cooper, J. A. G. (2004). Society and sea level rise. *science, 303*(5665), 1781-1782. Prandtl, L. (1926). Bemerkung zu dem Aufsatz von A. Einstein: Die Ursache der Mäanderbildung und das sogenannte Baersche Gesetz. *Naturwissenschaften, 14*(26), 619-620. Ren, M. E., & Shi, Y. L. (1986). Sediment discharge of the Yellow River (China) and its effect on the sedimentation of the Bohai and the Yellow Sea. *Continental Shelf Research, 6*(6), 785-810. Rhoads, B. L., & Kenworthy, S. T. (1995). Flow structure at an asymmetrical stream confluence. *Geomorphology, 11*(4), 273-293. Rinaldo, A., Fagherazzi, S., Lanzoni, S., Marani, M., & Dietrich, W. E. (1999a). Tidal networks 2. Watershed delineation and comparative network morphology. *Water Resources Research, 35*(12), 3905-3917. Rinaldo, A., Fagherazzi, S., Lanzoni, S., Marani, M., & Dietrich, W. E. (1999b). Tidal networks: 3. Landscape-forming discharges and studies in empirical geomorphic relationships. *Water Resources Research, 35*(12), 3919-3929. Rogers, K., & Woodroffe, C. D. (2015). Tidal Flats and Salt Marshes. In *Coastal Environments and Global Change* (pp. 227-250). Rozovskiĭ, I. L. v. (1957). *Flow of water in bends of open channels (in Russian)*: Academy of Sciences of the Ukrainian SSR.Schindfessel, L., Creëlle, S., & De Mulder, T. (2015). Flow Patterns in an Open Channel Confluence with Increasingly Dominant Tributary Inflow. *Water, 7*(9), 4724-4751. Schwarz, C., van Rees, F., Xie, D., Kleinhans, M. G., & van Maanen, B. (2022). Salt marshes create more extensive channel networks than mangroves. *Nature Communications, 13*(1), 2017. Sgarabotto, A., D'Alpaos, A., & Lanzoni, S. (2021). Effects of Vegetation, Sediment Supply and Sea Level Rise on the Morphodynamic Evolution of Tidal Channels. *Water Resources Research,*

57(7), e2020WR028577. Shi, B., Wang, Y. P., Du, X., Cooper, J. R., Li, P., Li, M. L., & Yang, Y. (2016). Field and theoretical investigation of sediment mass fluxes on an accretional coastal mudflat. *Journal of Hydro-environment Research, 11*, 75-90. Shi, B., Wang, Y. P., Wang, L. H., Li, P., Gao, J., Xing, F., & Chen, J. D. (2018). Great differences in the critical erosion threshold between surface and subsurface sediments: A field investigation of an intertidal mudflat, Jiangsu, China. *Estuarine, Coastal and Shelf Science, 206*, 76-86. Sisulak, C. F., & Dashtgard, S. E. (2012). Seasonal Controls On the Development And Character of Inclined Heterolithic Stratification In A Tide-Influenced, Fluvially Dominated Channel: Fraser River, Canada. *Journal of Sedimentary Research, 82*(4), 244-257. Solari, L., Seminara, G., Lanzoni, S., Marani, M., & Rinaldo, A. (2002). Sand bars in tidal channels Part 2. Tidal meanders. *Journal of Fluid Mechanics, 451*, 203-238. Somsook, K., Duka, M. A., Olap, N. A., Casila, J. C. C., & Yokoyama, K. (2020). Direct measurement of secondary circulation in a meandering macrotidal estuary. *Sci Total Environ, 739*, 139503. Somsook, K., Olap, N. A., Duka, M. A., Veerapaga, N., Shintani, T., & Yokoyama, K. (2022). Analysis of interaction between morphology and flow structure in a meandering macro-tidal estuary using 3-D hydrodynamic modeling. *Estuarine, Coastal and Shelf Science, 264*. Sullivan, J. C., Torres, R., Garrett, A., Blanton, J., Alexander, C., Robinson, M., et al. (2015). Complexity in salt marsh circulation for a semienclosed basin. *Journal of Geophysical Research: Earth Surface, 120*(10), 1973-1989. Temmerman, S., Meire, P., Bouma, T. J., Herman, P. M., Ysebaert, T., & De Vriend, H. J. (2013). Ecosystem-based coastal defence in the face of global change. *Nature, 504*(7478), 79-83. Termini, D., & Piraino, M. (2011). Experimental analysis of cross-sectional flow motion in a large amplitude meandering bend. *Earth Surface Processes and Landforms, 36*(2), 244-256. Thorne, C. R., Zevenbergen, L. W., Pitlick, J. C., Rais, S., Bradley, J. B., & Julien, P. Y. (1985). Direct measurements of secondary currents in a meandering sand-bed river. *Nature, 315*(6022), 746-747. Tu, J. B., Fan, D. D., Zhang, Y., & Voulgaris, G. (2019). Turbulence, Sediment-Induced Stratification, and Mixing Under Macrotidal Estuarine Conditions (Qiantang Estuary, China). *Journal of Geophysical Research: Oceans, 124*(6), 4058-4077. van Maanen, B., Coco, G., & Bryan, K. R. (2015). On the ecogeomorphological feedbacks that control tidal channel network evolution in a sandy mangrove setting. *Proc Math Phys Eng Sci, 471*(2180), 20150115. Vandenbruwaene, W., Schwarz, C., Bouma, T. J., Meire, P., & Temmerman, S. (2015). Landscape-scale flow patterns over a vegetated tidal marsh and an unvegetated tidal flat: Implications for the landform properties of the intertidal floodplain. *Geomorphology, 231*, 40-52. Voulgaris, G., & Meyers, S. T. (2004). Temporal variability of hydrodynamics, sediment concentration and sediment settling velocity in a tidal creek. *Continental Shelf Research, 24*(15), 1659-1683. Vousdoukas, M. I., Ranasinghe, R., Mentaschi, L., Plomaritis, T. A., Athanasiou, P., Luijendijk, A., & Feyen, L. (2020). Sandy coastlines under threat of erosion. *Nature Climate Change, 10*(3), 260-263. Wang, X. Y., & Ke, X. K. (1997). Grain-size characteristics of the extant tidal flat sediments along the Jiangsu coast, China. *Sedimentary Geology, 112*(1-2), 105-122. Wang, Y., & Zhu, D. K. (1990). Tidal flats of China (in

Chinsese). *Quaternary Sciences, 10*(4), 291-300. Wang, Y. P., Voulgaris, G., Li, Y., Yang, Y., Gao, J. H., Chen, J., & Gao, S. (2013). Sediment resuspension, flocculation, and settling in a macrotidal estuary. *Journal of Geophysical Research: Oceans, 118*(10), 5591-5608. Wells, J. T., Adams, C. E., Park, Y.-A., & Frankenberg, E. W. (1990). Morphology, sedimentology and tidal channel processes on a high-tide-range mudflat, west coast of South Korea. *Marine Geology, 95*(2), 111-130. Wilson, A. M., & Morris, J. T. (2012). The influence of tidal forcing on groundwater flow and nutrient exchange in a salt marsh-dominated estuary. *Biogeochemistry, 108*(1/3), 27-38. Xin, P., Wilson, A., Shen, C., Ge, Z., Moffett, K. B., Santos, I. R., et al. (2022). Surface Water and Groundwater Interactions in Salt Marshes and Their Impact on Plant Ecology and Coastal Biogeochemistry. *Reviews of Geophysics, 60*(1), e2021RG000740. https://doi.org/10.1029/2021RG000740Xing, F., Wang, Y. P., & Wang, H. V. (2012). Tidal hydrodynamics and fine-grained sediment transport on the radial sand ridge system in the southern Yellow Sea. *Marine Geology, 291-294*, 192-210. Xu, M., Meng, K., Zhao, Y., & Zhao, L. (2019). Sedimentary Environment Evolution in East China's Coastal Tidal Flats: The North Jiangsu Radial Sand Ridges. *Journal of Coastal Research, 35*(3), 524-533. Yang, S. L., Milliman, J. D., Xu, K. H., Deng, B., Zhang, X. Y., & Luo, X. X. (2014). Downstream sedimentary and geomorphic impacts of the Three Gorges Dam on the Yangtze River. *Earth-Science Reviews, 138*, 469-486. Zhao, K., Coco, G., Gong, Z., Darby, S. E., Lanzoni, S., Xu, F., et al. (2022). A Review on Bank Retreat: Mechanisms, Observations, and Modeling. *Reviews of Geophysics, 60*(2), e2021RG000761. https://doi.org/10.1029/2021RG000761Zhao, K., Gong, Z., Xu, F., Zhou, Z., Zhang, C. K., Perillo, G. M. E., & Coco, G. (2019). The Role of Collapsed Bank Soil on Tidal Channel Evolution: A Process-Based Model Involving Bank Collapse and Sediment Dynamics. *Water Resources Research, 55*(11), 9051-9071. Zhao, Y., Liu, Q., Huang, R., Pan, H., & Xu, M. (2020). Recent Evolution of Coastal Tidal Flats and the Impacts of Intensified Human Activities in the Modern Radial Sand Ridges, East China. *Int J Environ Res Public Health, 17*(9). Zhao, Y. Y., & Gao, S. (2015). Simulation of tidal flat sedimentation in response to typhoon—Induced storm surges: A case study from Rudong Coast, Jiangsu, China (in Chinsese). *Acta Sedimentologica Sinica, 33*(1), 79-90. Zhu, D. K., Ke, X., & Gao, S. (1986). Tidal flat sedimentation of Jiangsu coast (in Chinese). *J. Oceanogr. Huanghai Bohai Sea, 4*(3), 19-27.